Domains and defects in nuclear pasta

A. S. Schneider, M. E. Caplan, D. K. Berry, and C. J. Horowitz

Domains and defects in nuclear "pasta"

A. S. Schneider,[1, *] M. E. Caplan,[2, †] D. K. Berry,[3, ‡] and C. J. Horowitz[3, §]

[1] *TAPIR, Walter Burke Institute for Theoretical Physics, MC 350-17,*
California Institute of Technology, Pasadena, California 91125, USA
[2] *Department of Physics and McGill Space Institute, McGill University,*
3600 rue University, Montreal QC, Canada H3A 2T8
[3] *Center for Exploration of Energy and Matter and Department of Physics,*
Indiana University, Bloomington, IN 47405, USA
(Dated: October 12, 2018)

Nuclear pasta topology is an essential ingredient to determine transport properties in the inner crust of neutron stars. We perform semi-classical molecular dynamics simulations of nuclear pasta for proton fractions $Y_p = 0.30$ and $Y_p = 0.40$ near one third of nuclear saturation density, $n = 0.05 \, \mathrm{fm}^{-3}$, at a temperature $T = 1.0 \, \mathrm{MeV}$. Our simulations are, to our knowledge, the largest nuclear pasta simulations to date and contain up to $3\,276\,800$ nucleons in the $Y_p = 0.30$ and $819\,200$ nucleons in the $Y_p = 0.40$ case. An algorithm to determine which nucleons are part of a given sub-domain in the system is presented. By comparing runs of different sizes we study finite size effects, equilibration time, the formation of multiple domains and defects in the pasta structures, as well as the structure factor dependence on simulation size. Although we find qualitative agreement between the topological structure and the structure factors of runs with $51\,200$ nucleons and those with $819\,200$ nucleons or more, we show that simulations with hundreds of thousands of nucleons may be necessary to accurately predict pasta transport properties.

I. INTRODUCTION

At the base of the crust of neutrons stars (NSs) there is a dense system of nucleons immersed in a degenerate relativistic electron gas. Because of the high density, $\rho \approx 10^{14} \, \mathrm{g/cm}^3$, and Pauli blocking the degenerate electrons have a relatively long mean free path. Thus, electron transport dominates the system's electrical conductivity, thermal conductivity, and shear viscosity [1], although neutrons may have a non-negligible contribution [2]. Electron transport properties depend mainly on how electrons interact with protons. At the high densities found in the crust of NSs protons and neutrons may cluster into exotic non-spherical shapes known as nuclear pasta [3–6]. Hence, nuclear pasta topology determines transport properties at the base of the inner crust of NSs [7–14]. These exotic nuclear shapes also determine neutrino transport in non-trivial ways [11, 13–21], have an impact on core-collapse supernovae (CCSNe) [22–27], influence the structure and evolution of NSs [28–35] and their cooling curves [36–40], as well as affect the final state of matter ejected during binary neutron star mergers [41, 42]. Particularly, the presence of nuclear pasta may significantly alter the elastic properties of the inner crust of NSs. Thus, nuclear pasta may impact the lifetimes and size of mountains on NS crusts, which could produce continuous gravitational waves detectable by the Advanced LIGO and VIRGO detectors [43]. The elastic properties of nuclear pasta are the subject of a companion Letter [44].

Because nuclear pasta only exists under conditions achieved in the interior of NSs and during CCSNe, its existence can only be inferred through indirect means [11, 32, 37, 40] and its properties have to be studied via numerical simulations, such as molecular dynamics (MD). An overview of MD simualtions of nuclear pasta is presented by Caplan and Horowitz in Ref. [45]. Nuclear pasta is sensitive to temperature, density and proton fraction of the system [30, 46–55] and to yet unconstrained properties of nuclear matter [56–63]. Despite plenty of investigations using several different approaches a phase-diagram of nuclear pasta [64–71] and all of its possible topologies [65, 72–80] is still elusive. Amongst the issue faced are that analytical computations are limited to few symmetries [3, 56, 79, 80], numerical simulations that use simplified nucleon-nucleon potentials are constrained by finite size effects [12, 13, 42, 52, 81–83], while computational power is an impediment for detailed quantum approaches [55, 63]. Furthermore, strong magnetic fields such as the ones in NSs or produced during CCSNe may significantly alter the topology of the pasta [35, 84–86], but are rarely taken into account.

Another interesting aspect of the pasta phases is that their topology has equivalents in Skyrmion systems [87, 88], polymers [89–94], as well as in biological systems [95–97]. Past work has used nuclear pasta simulations to make insights into the physics of systems at completely different scales, such as biophysical membranes in eukaryotic cells [97]. This suggests that the structures formed by these self assembling systems are not dependent on the exact details of the microscopic interactions; rather, it may be possible to explain these commonalities with some simple universal geometric arguments.

Numerical simulations of nuclear pasta that incorpo-

* andschn@caltech.edu
† mecaplan@physics.mcgill.ca
‡ dkberry@iu.edu
§ horowit@indiana.edu

rate quantum mechanics are necessary to resolve detailed properties of the nucleons that make up the pasta. However, those calculations are computationally expensive and, to date, are limited to hundreds to a few thousand nucleons [24, 55, 63, 68]. Molecular dynamics (MD) simulations show that finite size effects and boundary conditions are important for such small simulations and influence the pasta shapes formed [42, 52, 83]. Moreover, to determine transport properties of nuclear pasta simulations with hundreds of thousands of nucleons or even more may be necessary [7, 9, 12, 14].

In this manuscript we discuss, to our knowledge, the largest nuclear pasta simulations to date. Using the Indiana University Molecular Dynamics (IUMD) code [12, 41, 98], we compare results for the topology and transport properties of nuclear pasta for simulations containing up to $3\,276\,800$ nucleons for proton fractions of $Y_p = 0.30$ and $819\,200$ for $Y_p = 0.40$. We also discuss a method to discriminate domains within the simulation volume and examine how these evolve over time. In Sec. II we review our MD formalism, discuss code performance, as well as present our algorithms to compute structure factors from our MD simulations and to differentiate domains within the simulation volume. We present our results for $Y_p = 0.30$ systems in Sec. III and for $Y_p = 0.40$ systems in Sec. III B. We conclude and discuss present challenges in Sec. IV.

II. FORMALISM

The formalism of our molecular dynamics (MD) study is the same of many previous works initiated by Horowitz *et al.* [7]. For a review refer to Ref. [45] and references therein. In our MD simulations we model nucleons as point-like particles immersed in a background electron gas. We consider N nucleons, N_p protons and N_n neutrons such that $N = N_p + N_n$, inside cubic volumes of side L with periodic boundary conditions. The number density of the system is $n = N/L^3$ while its proton fraction is $Y_p = N_p/N$. Nucleons interact via a two-body force limited to the the nearest periodic image of other nucleons. The interaction potential depends on nucleon isospins and their inter-particle distances r and has the form

$$V_{np}(r) = ae^{-r^2/\Lambda} + [b - c]e^{-r^2/2\Lambda}, \tag{1a}$$

$$V_{nn}(r) = ae^{-r^2/\Lambda} + [b + c]e^{-r^2/2\Lambda}, \tag{1b}$$

$$V_{pp}(r) = ae^{-r^2/\Lambda} + [b + c]e^{-r^2/2\Lambda} + \frac{\alpha}{r}e^{-r/\lambda}. \tag{1c}$$

The subscripts n and p denote, respectively, whether a nucleon is a neutron or a proton. The parameters $a = 110\,\mathrm{MeV}$, $b = -26\,\mathrm{MeV}$, $c = 24\,\mathrm{MeV}$ and $\Lambda = 1.25\,\mathrm{fm}^2$ were fit to reproduce some properties of finite nuclei, pure neutron matter and symmetric nuclear matter [7]. Meanwhile, α is the fine structure constant. The long-range Coulomb repulsion between protons is screened by the

background electron gas which renders the system electrically neutral. The relativistic Thomas-Fermi screening length λ is given by

$$\lambda = \frac{\pi^{1/2}}{2\alpha^{1/2}} \left(k_F \sqrt{k_F^2 + m_e^2} \right)^{-1/2} \tag{2}$$

where $k_F = (3\pi^2 n_e)^{1/3}$ is the Fermi momentum of electrons with density n_e and mass m_e. For electrically neutral systems $n_e = Y_p n$. As in previous works we set the screening length λ to 10 fm. For the proton fractions considered in this work this value is somewhat shorter than the value obtained considering non-interacting relativistic electrons, Eq. (2). However, we do not expect this difference to significantly influence our results [12, 13].

Using this formalism, we simulate twelve systems at a constant density $n = 0.05\,\mathrm{fm}^{-3}$, approximately one-third of nuclear saturation density, and constant temperature $T = 1\,\mathrm{MeV}$. Five of runs have proton fraction $Y_p = 0.30$ and contain $51\,200$, $409\,600$, $819\,200$, $1\,638\,400$, and $3\,276\,800$ nucleons. These runs are discussed in Sec. III A. Seven runs have proton fraction $Y_p = 0.40$, and contain $51\,200$, $61\,440$, $76\,800$, $102\,400$, $204\,800$, $409\,600$, and $819\,200$ nucleons. These are discussed in Sec. III B.

A. The IUMD code performance

Our MD simulations were run on the Big Red 2 supercomputer at Indiana University and on the Titan supercomputer at Oak Ridge National Laboratory. Runs were performed using the IUMD CPU/GPU hybrid code described in Refs. [12, 41, 98]. Appropriate understanding of code performance and its limitations play a large role in determining the feasibility of state-of-the-art runs. Tracking bottlenecks in the code and causes for performance variability and degradation over time is an important factor in optimizing the usage of resources. Therefore, here we review some code details and examine its performance for our simulations with proton fraction $Y_p = 0.30$.

In the IUMD code short range nuclear forces are computed on CPUs using a neighbor list scheme where only nucleons within 11 fm of each other interact. Hence, computation of nuclear forces scales with $\mathcal{O}(N)$. Meanwhile, long range Coulomb interaction between protons is distributed across the GPUs and scales as $\mathcal{O}(Y_p^2 N^2)$. We recall that the Coulomb force is screened by background electrons. In the simulations performed in this work we have chosen $\lambda = 10\,\mathrm{fm}$, slightly smaller than the expected values for the proton fractions we use [12]. For screened systems it is often necessary to treat interactions between pairs of charged particles separated up to distances of at least 8λ [99]. Thus, for the larger simulations presented in our work, where the size of the box is larger than 160 fm, the introduction of a cut-off radius would prevent force calculations between pairs of protons separated by distances greater than 8λ. This is implemented in the

CPU version of the IUMD code. Nevertheless, when using GPUs this approach becomes counterproductive since GPUs perform significantly better when all processing units are performing the same operations simultaneously. Tracking proton-proton neighbor lists would also prevent the often unecessary calculations between distant pairs of protons. Yet, the issue with this approach lies in the limited memory available in each processing unit as each proton may interact with a hundreds thousand other protons. Robust fast-multipole methods for Yukawa-type potentials tackle both of these issues, see Refs. [100–102], and should be implemented and tested in future works that have the goal of studying large pasta systems. However, these methods are yet to be implemented and tested in the IUMD code. Thus, for large systems, such as the ones considered in this work, the bulk of the computational time is spent computing Coulomb forces. Thus, a simulation time step should be, to a good approximation, proportional to $(Y_pN)^2/P$, where Y_p is the proton fraction N the number of nucleons and P the number of CPU/GPU units used. For an early discussion on the code scalability using only Coulomb interactions we refer to Berry $et\ al.$ [98].

In Fig. 1 we plot the code performance $\xi = k_\xi(Y_pN)^2/(P\tau)$ for our $Y_p = 0.30$ simulations with $N = 409\,600$ nucleons as well as $2N$, $4N$, and $8N$ nucleons. Here, k_ξ is a proportionality constant and τ the real time necessary to compute a simulation time step. Ideally, the value of ξ should remain constant across simulations of different sizes and throughout each run. However, we observe differences that depend on the simulation size, number of computing nodes used, and on the compiler version used to compile the IUMD code.
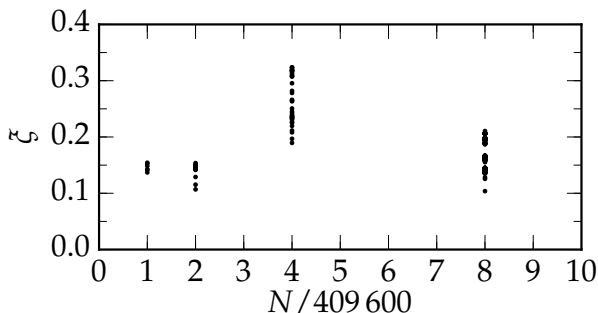

FIG. 1. Plot of the performance factor $\xi = k_\xi(Y_pN)^2/(P\tau)$ for our runs with N nucleons and proton fraction $Y_p = 0.30$. The larger ξ the better the performance. Note that ξ is normalized to an arbitrary value as only ratios between different ξs are meaningful.

The $409\,800$ nucleons run was performed on the hybrid CPU/GPU nodes of the Big Red 2 supercomputer. Within this run the number of CPU/GPU nodes was chosen to be either 64, 80, 100, or 128. The entirety of this run was performed using the IUMD code compiled with PGI compiler version 14.1. We observed an approximate 5, 10, and 15% decrease in code performance (ξ) as the number of nodes requested were increased, respectively, from 64 to 80, 100, and 128.

The runs with $819\,200$ and $1\,638\,400$ nucleons were performed exclusively using 1024 nodes on the hybrid CPU/GPU nodes of the Titan supercomputer. Although both Titan and Big Red 2 have NVIDIA Tesla GPU Accelerators, Titan is equipped with the K20X model while Big Red 2 is equipped with the K20 model. Thus, since Titan GPUs have a slightly larger number of CUDA cores (2688 to 2496) and faster base clock (732 to 706 MHz) than Big Red 2 GPUs, this should translate into better performance. However, comparing the results of the $409\,800$ and $819\,200$ runs, we note that the performance of the smaller run is on average slightly better. This is likely due to the use of an excessive number of nodes in the $819\,200$ nucleon run, which degraded performance. This is clear from the fact that the $1\,638\,400$ nucleon run performs significantly better than both the $409\,800$ and the $819\,200$ nucleon runs.

We noticed significant performance changes throughout the Titan runs, with $0.10 \lesssim \xi \lesssim 0.16$ for the $819\,200$ nucleon run and $0.19 \lesssim \xi \lesssim 0.33$ for the $1\,638\,400$ nucleon run. In parts of the run the variability in performance could be tracked down to unusually slow MPI communication times between the requested nodes, while in other cases variability was due to small improvements in the IUMD code that were implemented during early stages of these two runs. However, the main aspect dictating the variability in code performance was the compiler version used. The IUMD code performs best when compiled with the PGI compiler version 14.1. This compiler version boosts the performance by at least 25% when compared to any of the other eight PGI compiler versions tried, most of them more recent versions than 14.1.

Our largest run, with $3\,276\,800$ nucleons, was performed exclusively on the Big Red 2 supercomputer. The number of nodes used was modified throughout the run and changed between 64, 128, 256, and 512, depending on machine availability. Due to the large number of nucleons in this run, we did not observe changes in performance of more than 10% by altering the number of nodes used from 64 to 512, a factor of eight. As was the case for the Titan runs, the most significant determinant in code performance was the PGI compiler version used. Again, the PGI CUDA Fortran compiler version 14.1 significantly outperformed any of the other versions tried.

B. Structure factor

Nuclear pasta shapes are relevant in astrophysical scenarios as they determine neutrino transport in core-collapse supernovae (CCSNe) and cooling time-scales of neutron stars (NSs) [7, 11, 14, 17, 24, 26, 66, 68, 103] as well as NS crust properties [13, 31, 32]. Transport properties such as viscosity and electrical and heat conductivity are a function of the structure factor of the pasta shapes [7, 13, 14, 19]. Thus, one of our interests is

to compute if and how structure factors may be affected between simulations that differ by orders of magnitude in the number of nucleons.

At different points of our simulations we obtain a trajectory file of all nucleons by saving their positions every $200 \, \mathrm{fm}/c$ for $10^6 \, \mathrm{fm}/c$. We use these trajectory files to determine nucleon structure factors following Refs. [10, 12–14, 50] and reviewed below. The structure factor $S_i(\boldsymbol{q})$ for a given transferred momentum $\boldsymbol{q}$ for a nucleon of type $i = n, p$ is given by the time average of the nucleon density in momentum space:

$$S_i(\boldsymbol{q}) = \langle \rho_i^\star(\boldsymbol{q}, t) \rho_i(\boldsymbol{q}, t) \rangle_t - \langle \rho_i^\star(\boldsymbol{q}, t) \rangle_t \langle \rho_i(\boldsymbol{q}, t) \rangle_t. \quad (3)$$

Above, $\rho_i(\boldsymbol{q}, t) = N_i^{-1/2} \sum_{j=1}^{N_i} e^{i\boldsymbol{q}\cdot\boldsymbol{r}_j(t)}$ is the nucleon density in momentum space, $\rho^\star(\boldsymbol{q}, t)$ its complex conjugate, with N_i the number of nucleons of type i, $\boldsymbol{r}_j(t)$ the position of the j-th nucleon of type i at time t, and the angled brackets $\langle A \rangle_a$ denote the average of quantity A over a set of a. To avoid finite-size effects in the computations of $\rho_i(\boldsymbol{q}, t)$ due to the periodic boundary conditions imposed in the system we only take into account momenta $\boldsymbol{q}$ such that

$$\boldsymbol{q} = 2\pi \left(\frac{n_x}{L_x}, \frac{n_y}{L_y}, \frac{n_z}{L_z} \right), \quad (4)$$

where n_i are integers and L_i is the size of the box along the i direction [10, 12–14, 50]. Recall that in this work we consider cubic boxes and, thus, $L_x = L_y = L_z = L$.

C. Domains and defects

All systems simulated for this work have a constant number density $n = 0.05 \, \mathrm{fm}^{-3}$, constant temperature $T = 1 \, \mathrm{MeV}$, and proton fractions of either $Y_p = 0.30$ or $Y_p = 0.40$. As discussed in Fig. 1 of Ref. [97] for a $Y_p = 0.40$ system with $40\,000$ nucleons, protons and neutrons in the simulation volume initially bind locally due to the short-range nuclear attraction to form high density filaments. Over time, fluctuations due to the Coulomb repulsion introduce long-range correlations in the system and the filaments rearrange themselves. For systems with proton fraction $Y_p = 0.30$ parallel plates perforated by an hexagonal arrangement of circular holes, the "waffle" phase [12], form. Meanwhile, for proton fraction $Y_p = 0.40$ the system arranges itself in parallel plates connected by helical ramps, known "parking garage" structures [97]. The "waffle" phase [12], is similar to hexagonal networks seen in some phospholipid systems [89, 90, 104], while the "parking garage" structure analog in lipid systems is known as Terasaki ramps [95, 96].

The equilibration time of an MD system simulated at constant density, temperature, and proton fraction is correlated with the number of nucleons in the simulation volume, but depends in non-trivial ways on the proton fraction. As in previous works, we loosely define equilibrium as convergence of the mean and Gaussian curvatures of the system [12, 13]. Systems with a few thousand nucleons equilibrate rather quickly, while systems with hundreds of thousands to millions of nucleons take a significant amount of time to equilibrate. Some works suggest that different pasta phases may coexist [63, 73, 105], however, we do not observe that in any of our runs. Nonetheless, for volumes large enough we observed that the plates formed in our simulations could be oriented across multiple directions, i.e., some runs exhibited more than one domain. To determine the formation time of domains and whether they were stable or eventually all merged into a single domain we implemented an algorithm to examine to which domain each proton in the simulation belonged to. This algorithm, discussed next, can be easily extended to include the neutrons. Since in the runs performed in this work most neutrons are highly correlated with protons while only a few form a low density background gas we do not include any neutrons in our analysis for the sake of speed. Furthermore, for very low proton fractions many or most of the neutrons drip out of the pasta structures to form a background gas. In this case only some of the neutrons are correlated with the protons.

The first step in our algorithm is to compute the proton *elastic* structure factor $S_p^e(\boldsymbol{q}) = \langle \rho_i^\star(\boldsymbol{q}, t) \rho_i(\boldsymbol{q}, t) \rangle_t$, i.e., the first right-hand-side term in Eq. (3). The time average is performed over the last $10^6 \, \mathrm{fm}/c$ of each run. For the topologies studied in this work $S_p^e(\boldsymbol{q})$ is much larger than the angle average $S_p^e(q) = \langle S_p^e(\boldsymbol{q}) \rangle_{|q|}$ whenever $\boldsymbol{q}$ is parallel to a direction normal to one of the plates formed. Mathematically, $S_p^e(\boldsymbol{q}) \gg \langle S_p^e(\boldsymbol{q}) \rangle_{q=|q|} \Leftrightarrow \boldsymbol{q} \parallel \boldsymbol{n}_{\mathrm{plates}}$, where $\boldsymbol{n}_{\mathrm{plates}}$ is the direction normal to the plates (domains) in the system. If there is more than one domain, there will be multiple $\boldsymbol{n}_{i,\mathrm{plates}}$ and as many $\boldsymbol{q}_i$ that satisfy $S_p^e(\boldsymbol{q}_i) \gg S_p^e(q)$ where the $\boldsymbol{q}_i \parallel \boldsymbol{n}_{i,\mathrm{plates}}$. We note that the magnitude of $q = |\boldsymbol{q}| \approx 2\pi/d$, where d is the average distance between nucleons in neighboring plates [12, 13].

Once we have determined a set of momenta $\boldsymbol{q}_i = 2\pi(n_x'/L_x, n_y'/L_y, n_z'/L_z)$ such that $S_p^e(\boldsymbol{q}') \gg S_p^e(q)$, we compute a separate elastic structure factor for each proton j in the system for each $\boldsymbol{q}_i$, i.e.,

$$\mathcal{S}_j(\boldsymbol{q}_i, t) = \rho_j^\star(\boldsymbol{q}_i, t) \rho_j(\boldsymbol{q}_i, t) \quad (5)$$

where

$$\rho_j(\boldsymbol{q}_i, t) = \frac{1}{\sqrt{\mathcal{N}_j(t)}} \sum_{k=1}^{\mathcal{N}_j(t)} e^{i\boldsymbol{q}_i \cdot (\boldsymbol{r}_j(t) - \boldsymbol{r}_k(t))}. \quad (6)$$

Here, how much larger $S_p^e(\boldsymbol{q}')$ is compared to $S_p^e(q)$ is a choice made by convenience and related to the number of domains we want to track or show. Typically, we try show domains q' that satisfy $S_p^e(\boldsymbol{q}') \gtrsim 300 S_p^e(q)$ either half-way through the run or at the end of it. However, that choice is not strict and sometimes we increase the threshold to show a smaller number of domains, as in the case of the $3\,276\,800$ nucleon run. Note that the subscripts j in ρ_j in Eqs. (5) and (6) are labels for each proton and not for nucleon type as in Sec. II B. The sum in k above only

runs over the $\mathcal{N}_j(t)$ neighboring protons of j at time t. The neighbors are defined as

$$k \in \mathcal{N}_j(t) \Leftrightarrow \begin{cases} |x_j(t) - x_k(t)| \le |L_x/2n'_x|, \\ |y_j(t) - y_k(t)| \le |L_y/2n'_y|, \\ |z_j(t) - z_k(t)| \le |L_z/2n'_z|. \end{cases} \quad (7)$$

where $r_j(t) = (x_j(t), y_j(t), z_j(t))$ and similar for the index k. In cases where one or two of the $n'_w = 0$, where $w = x$, y, or z, we set $n'_w \to 10$ in the computations of the neighbor list only. This choice does not significantly affect $\mathcal{S}_j(\boldsymbol{q}_i, t)$ since, $n'_w = 0$ if and only if there are no long range correlations along the w direction(s).

After computing $\mathcal{S}_j(\boldsymbol{q}_i, t)$ we assign a proton j to domain D_i for which $\mathcal{S}_j(\boldsymbol{q}_i, t)$ is a maximum; unless it falls below a threshold, in which case it is set to the defects domain D_0.

A two dimensional example of our algorithm is shown in Fig 2. The system has periodic boundary conditions and its particles arranged themselves into two separate domains. For region R_1, defined by $-L/6 \le x \le +L/2$, most particles form planes normal to the vector $\boldsymbol{n}_1 = (-L/3, L/6)$. For particles r belonging to those planes the momentum transfer that maximizes $S_r(q)$ (here the time variable t is omitted for clarity) is $\boldsymbol{q}_1 = \frac{2\pi}{L}(-3, 6)$. One such example is shown by the particle tagged in yellow in the top panel of Fig. 2. Its $\mathcal{N}_r$ neighbors are the ones inside the yellow box, which can be regarded approximately as a unit cell for the planes in R_1. Thus, for most particles in R_1 $\mathcal{S}_r(\boldsymbol{q}_1) \gg \mathcal{S}_r(\boldsymbol{q}_{i \ne 1})$ and we set them as being part of domain D_1.

Performing a similar analysis for the particles l in the region R_2 defined by $-L/2 \le x \le -L/6$ we obtain that the planes formed are normal to the vector $\boldsymbol{n}_2 = (-L/6, L/6)$. Thus, for particles in R_2 we obtain that $\mathcal{S}_l(\boldsymbol{q}_2) \gg \mathcal{S}_l(\boldsymbol{q}_{i \ne 2})$ if and only if we set $\boldsymbol{q}_2 = \frac{2\pi}{L}(-6, 6)$. These particles form domain D_2. One such particle is tagged in light-blue in the top panel of Fig. 2 and its $\mathcal{N}_l$ neighbors are the particles inside the light-blue box.

Exceptions happen for particles t near transition regions between different domains. For those particles, both $\mathcal{S}_t(\boldsymbol{q}_i)$ may have similar values. We identify the particle as belonging to the domain D_i that produces the larger $\mathcal{S}_t(\boldsymbol{q}_i)$, unless this maxima is below a threshold value. The threshold value is adjusted so that at the end of each run the number of particles that are on the "defects" domain D_0 is small while at the same time guarantees that the domains D_i are clearly identified.

The method described above proved very accurate to identify different domains in our simulations. Its main limitation is that, due to thermal fluctuations of the domains, the angle θ_{ij} between the normal that defines two domains i and j has to be such that $\theta_{ij} \gtrsim 5°$. If that constraint is not imposed, often particles in domain D_i (D_j) are misidentified as being part of D_j (D_i).

In the bottom panel of Fig. 2 we color all particles according to the domain they belong following our algorithm. Two domains are clearly identified with particles that form their interface being identified as "defects".
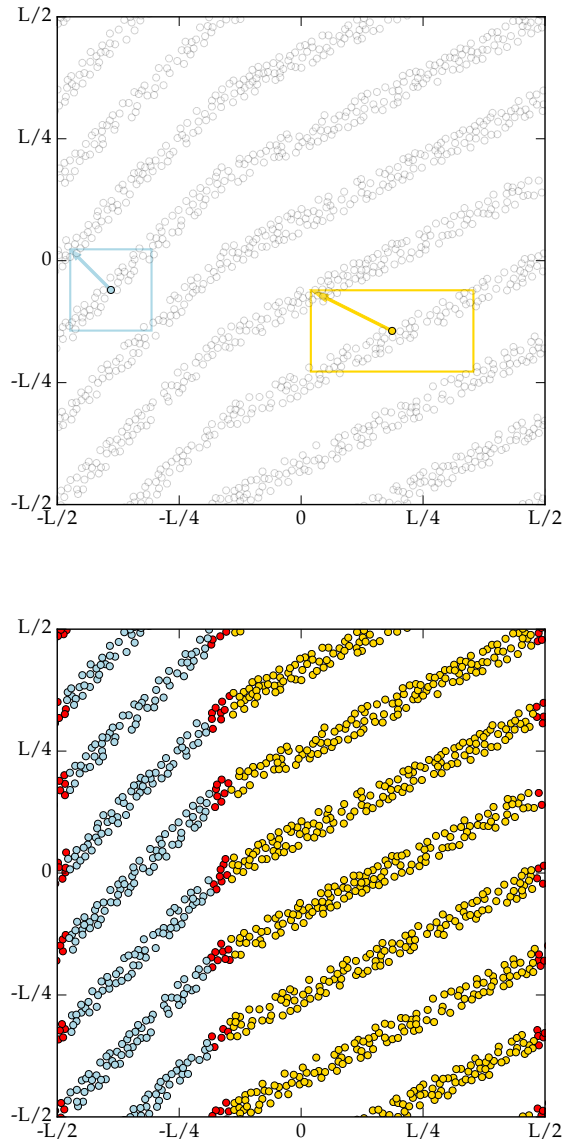

FIG. 2. (Color online) Two dimensional example of our domain recognition algorithm. On the top we identify two particles that belong to each of the two domains formed, see text. On the bottom we color each particle according to the domain they belong to: red for defects domain D_0, yellow for domain D_1, identified by the vector $\boldsymbol{q}_1 = \frac{2\pi}{L}(-3, 6)$, and light blue for domain D_2, identified by the vector $\boldsymbol{q}_2 = \frac{2\pi}{L}(-6, 6)$.

Although we only discuss cubic volumes in this work, the algorithm was presented in the more general framework of cuboids since it is used in the companion paper, Ref. [44], to study the breaking mechanism of nuclear pasta under extreme deformations.

III. RESULTS

We discuss the results for our molecular dynamics (MD) simulations with proton fractions $Y_p = 0.30$, Sec. III A, and $Y_p = 0.40$, Sec. III B. As in most of our previous works, the runs are perfomed at a temperature $T = 1.0$ MeV.

We comment on the choices of proton fractions and temperatures used in our simulations. The values used here are larger than what is realized in cold catalyzed crusts of neutron stars (NSs). These relatively high temperature and proton fractions are chosen for a few reasons. First, our semiclassical model has no explicit quantum zero-point motion. Thus, its predictions will be unrealistic at the very low temperatures found, 0.01 MeV (10^8 K), in cooled NS crusts. Furthermore, in our semi-classical neutrons and protons freeze in place for temperatures T   0.5 MeV, similar to what is reported by Dorso *et al.* in Ref. [51]. At temperatures of approximately $T \approx 1.5$ MeV the structures formed quickly melt. Therefore, we simulate the system at temperature $T = 1.0$ MeV. This temperature is large enough to guarantee that the topology of the system will evolve during the simulations, yet low enough so that the system forms structures with long range correlations that last for long times [12]. The large proton fractions, compared to $Y_p \lesssim 0.10$ expected in the NS crust, is set for similar reasons. For proton fractions $Y_p \lesssim 0.25$ our semi-classical system does not form long range structures, although those are predicted using different models for the conditions found in the crusts of cool NSs [74, 106]. Mainly, we are interested in the topological structures formed more than in the physical conditions needed to produce them within the framework of our semi-classical model.

A. Simulations with $Y_p = 0.30$

We start examining five runs with proton fraction $Y_p = 0.30$. Two of these runs, the ones containing 51 200 and 409 600 nucleons, have already been presented under a different light in Ref. [12]. We add to those two, three larger simulations containing 819 200, 1 638 400, and 3 276 800 nucleons. A summary of the runs is shown in Table I.

We reiterate that all of our runs are performed within a cubic volume with constant nucleon number density $n = 0.05$ fm^{-3}, temperature $T = 1$ MeV, and fixed screening length $\lambda = 10$ fm. Under these conditions all simulations with proton fraction $Y_p = 0.30$ converged to the expected "waffle" phase [12]. This same phase has been obtained by Sbille *et al.*, albeit at a different proton fraction, by solving the equations of motion of single particle wave functions spanned in a wavelet basis where nucleons interact via a zero-range effective interaction [107]. Sagert *et al.* also see the waffle phase from self-consistent Skyrme Hartree-Fock (SHF) calculations [55]. However, in Sagert *et al.* the initial conditions for their SHF com-

TABLE I. Summary of our MD runs with $Y_p = 0.30$. We list the number of nucleons in the first column, the side length of the simulation cube on the second column, the total evolution time in the third column, and the number of domains observed at the end of the run in the fourth column. In the last column +1 denotes that there is still a "defects" domain at the end of the run, see text and Figs. 7, 10 and 13.

Nucleons	t_{total} (10^6 fm/c)	L_{box} (fm)	Domains
51 200	31.0	100.8	1
409 600	32.5	201.6	1
819 200	55.0	254.0	1+1
1 638 400	37.0	320.0	1
3 276 800	32.0	403.2	6+1

putation was obtained from the final configuration of an MD run. Thus, it is unclear if the final configuration in their simulations is a stable or meta-stable state.

The topology of nuclear pasta is often characterized by its Minkowski functionals, see Refs. [12, 49, 50, 65, 70–72]. Specifically, the mean and Gaussian curvatures tell us about the degree of connectivity of the structures formed [49, 70]. In Fig. 3 we show the mean curvature B and Gaussian curvature χ normalized by the surface area A of the system for the $Y_p = 0.30$ simulations. Technical details on how we compute Minkowski functionals are discussed in Refs. [12, 50]. The curvatures of all our simulations follow a similar pattern and results for the three new large simulations agree qualitatively with the two smaller ones[1]. However, it is unclear whether any quantitative differences in the curvature are due to finite size effects or the presence of defects and/or multiple domains in the simulation. Furthermore, the 819 200 simulations seems to go through a phase rearrangement between 40 and 44×10^6 fm/c where the curvatures deviate from their average values. This deviation is similar to that what is observed for the bond angle metric Q_6 and the diffusion coefficient of ions in Coulomb crystals as it freezes [108].

Besides the average curvatures, another important quantity to measure from these large simulations is the structure factor of each topology as they encode the transport properties of the pasta phases [1, 2, 7, 10, 11, 13, 14, 49, 103]. We follow our previous work [13] and compute the proton structure factors $S_p(\boldsymbol{q})$ for possible values of $\boldsymbol{q}$ within our periodic simulation box, Eq. (4). If we assume that pasta has multiple uncorrelated domains it is convenient to describe its structure factor as an average over all momentum transfers with same magnitude $q = |\boldsymbol{q}|$, *i.e.*, obtain $S_p(q) = \langle S_p(\boldsymbol{q}) \rangle_q$ [7, 14, 50].

---

[1] Due to a system purge of the Titan supercomputer files and incomplete backup of our data configurations for the 819 200 nucleon run before 18×10^6 fm/c and 1 638 400 before 6×10^6 fm/c were lost and, thus, not plotted.
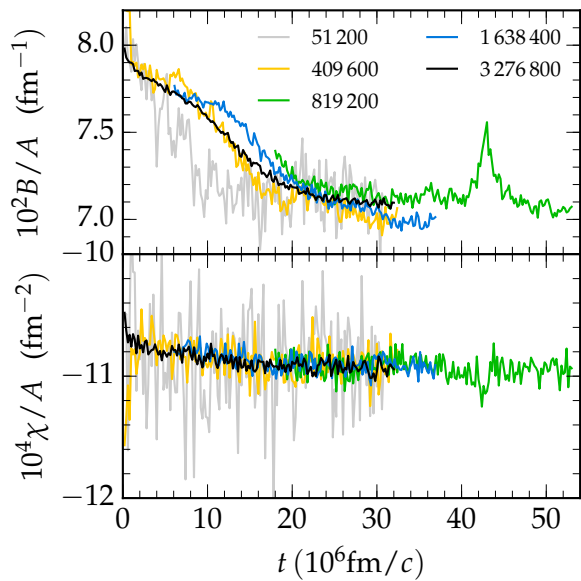
FIG. 3.   (Color online) Plots of the normalized mean curvature B/A (top) and normalized mean Gaussian curvature χ/A (bottom) as a function of simulation time t for four simulations with $Y_p = 0.30$, $n = 0.05\,\mathrm{fm}^{-3}$ and $T = 1.0\,\mathrm{MeV}$.

It is also possible that domains with different orientations are only stable when separated by distances larger than the size of our simulation volume and, thus, even though our simulations may only show a single domain, the relevant quantity is still the angle averaged quantity $S_p(q)$. However, it may be that the pasta phases are in fact anisotropic over very large length scales or that its defects are correlated [11, 13] and, thus, the anisotropy in $S_p(\boldsymbol{q})$ does affect its transport properties. In Fig. 4 we show the angular average structure factor for protons $S_p(q)$ and its upper and lower bounds, defined by the maxima and the minima in $S_p(\boldsymbol{q})$ for a given $q = |\boldsymbol{q}|$.

By comparing the results of simulations of different sizes, it is clear that the 51 200 nucleon run is too small to reproduce some of the quantitative features in $S_p(\boldsymbol{q})$ seen in the larger runs[2]. The most obvious differences are the lower number and smaller magnitude of peaks in the 51 200 nucleon run. This may be due to a couple of factors such as the finite size of the simulation or the formation of multiple mostly independent domains in the simulation volume. However, we have shown in Fig. 3 of Ref. [12] that the 51 200 nucleon simulation forms only a single domain. Furthermore, we will show below that three of the four simulations with more than 51 200 nucleons form a single dominant domain at the

---

[2] An error in the $S_p(\boldsymbol{q})$ code used in Ref. [12] was corrected. Although results in Ref. [12] are qualitatively correct, the error changes the magnitude of some of the peaks in $S_p(q)$ discussed in that work and, thus, direct comparison of those results and the ones presented here is not possible.
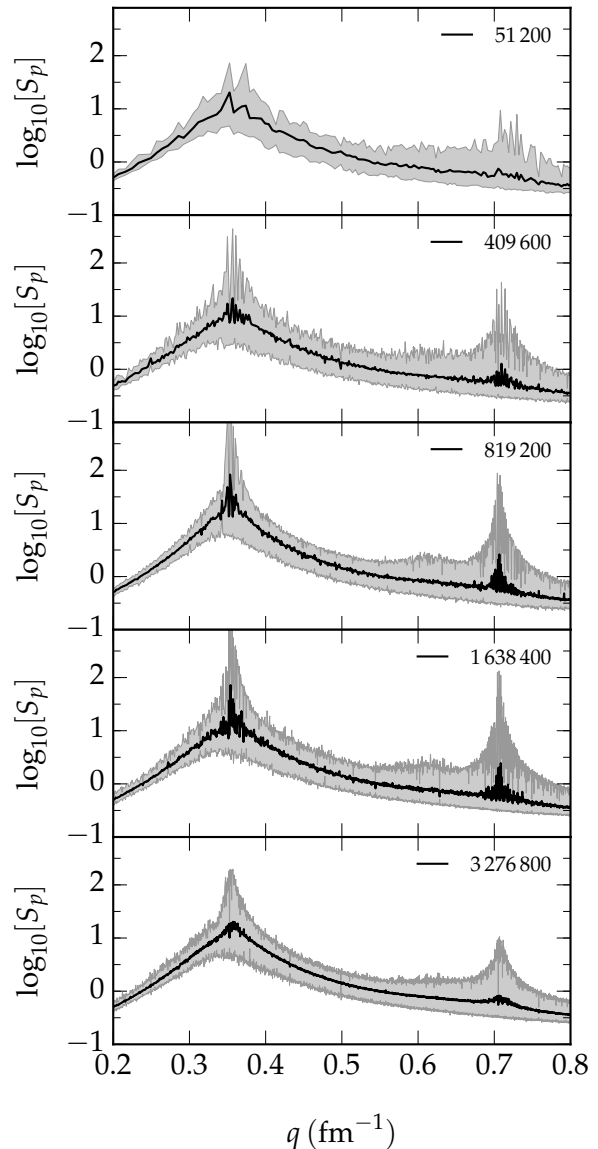

FIG. 4.   Plots of the angle averaged proton structure factor $S_p(q) = \langle S_p(\boldsymbol{q}) \rangle_q$ (thick black lines) for the final $1.0 \times 10^6\,\mathrm{fm}/c$ of each simulation. The average value is bound by the maximum and minimum in $S_p(\boldsymbol{q})$ for each $q = |\boldsymbol{q}|$ (shaded grey area).

end of the run. Therefore, the culprit of the differences seen between $S_p(\boldsymbol{q})$ for the 51 200 simulation and the larger ones is the simulation size. If this is the case, it introduces a severe constraint in the computations of transport properties of nuclear pasta. Even though MD simulations containing 51 200 nucleons can now be easily achieved with the IUMD code, quantum molecular dynamics (QMD) simulations, which use more sophisticated interaction potentials between nucleons [14, 25], as well as quantum-mechanical state-of-the-art pasta simulations [55, 63, 71], which rely on energy density func-

tional calculations, are still limited, to a few dozen thousand nucleons or much less. For example, recently, Nandi and Schramm computed structure factors and Coulomb logarithms from QMD simulations for a range of densities, temperatures, and proton fractions [14]. All of their simulations contain $8\,192$ to $16\,384$ nucleons. Assuming our results also hold for simulations that use different nucleon-nucleon interactions, it is likely that the results for transport properties of Nandi and Schramm still suffer from considerable finite size effects. Nevertheless, it is encouraging that there is a very good qualitative agreement between their results for the structure factor $S_p(q)$ and ours for $Y_p = 0.30$, $n \approx 0.5\,\mathrm{fm}^{-3}$ at $T = 1\,\mathrm{MeV}$.

As we increase the number of nucleons from $51\,200$ nucleons to $409\,600$ the box length along each direction doubles and, therefore, the number of vectors $\boldsymbol{q}$ to be analyzed as well as the statistical significance of our results increase by a factor of $\sqrt{8}$. The magnitudes of the peaks in $S_p(\boldsymbol{q})$ as well as the number of oscillations in both $S_p(\boldsymbol{q})$ and $S_p(q)$ near $q' \approx 0.36\,\mathrm{fm}^{-1}$ and $q'' \approx 2q'$ increase considerably with a larger simulation[3].

By increasing further the simulation volume, to $819\,200$ nucleons, the maxima in $S_p(\boldsymbol{q})$ and its average $S_p(q)$ increase even more in magnitude near q' and q''. However, there is little quantitative difference between $S_p(\boldsymbol{q})$ and $S_p(q)$ between the runs with to $819\,200$ and $1\,638\,400$ nucleons.

In our largest run, with $3\,276\,800$ nucleons, the structure factor $S_p(\boldsymbol{q})$ is qualitatively very similar to the ones computed for the smaller simulations. The peaks in $S_p(\boldsymbol{q})$ for this run, however, are somewhat smaller than the ones for the $819\,200$ and $1\,638\,400$ nucleon runs. We show below that this is likely not due to finite size effects, which should be well constrained in a simulation of this size, but due to this simulation having multiple large domains in the time we analyzed its structure factor. This is unlike the smaller simulations, which by the end of the run show a single large domain, which occupies almost all of the simulation volume.

Despite the seemingly convergence of the curvatures, an interesting question to ask is whether the simulated systems, once evolved for a long time, are arranged into a single domain or multiple ones. We use the methods of Secs. II B and II C to identify the main domain(s) in each run. These are discussed in detail for the three new simulations ran for this work.

1. Simulation with $819\,200$ nucleons

From all of our simulations, the one with $819\,200$ nucleons and proton fraction $Y_p = 0.30$ was the one evolved

---

[3] The magnitude $q' \approx 2\pi/d$ is directly related to the average distance d between nucleons in neighboring plates in the simulation volume.

for the longest time, about $55 \times 10^6\,\mathrm{fm}/c$. This run cost approximately 2.5×10^5 node hours on the hybrid CPU/GPU nodes of the Titan supercomputer.
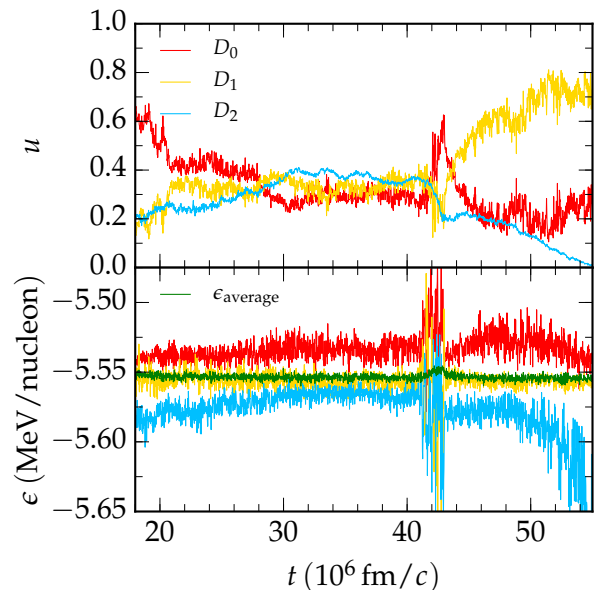

FIG. 5. (Color online) Volume fraction u (top) and potential energy per nucleon ϵ (bottom) for each domain in the system for the $819\,200$ nucleon simulation as a function of simulation time. The three domains are D_0 (defects), D_1 ($\boldsymbol{q}_1 = \frac{2\pi}{L}(-1, 2, 14)$), and D_2 ($\boldsymbol{q}_2 = \frac{2\pi}{L}(-8, 9, 8)$). Green line in the bottom pane is the average system energy. We note that due to a system purge of Titan files and incomplete backup of our data configurations for the $819\,200$ nucleon run before $18 \times 10^6\,\mathrm{fm}/c$ were lost.

In Fig. 5 we plot the volume fraction u and energy per nucleon ϵ of two domains identified in the system in addition to a "defects" domain. Domains D_1 and D_2 are defined, respectively by the momenta $\boldsymbol{q}_1 = \frac{2\pi}{L}(-1, 2, 14)$ and $\boldsymbol{q}_2 = \frac{2\pi}{L}(-8, 9, 8)$ where $L = 240\,\mathrm{fm}$. We also define domain D_0 as the group of nucleons that are not part of either D_1 nor D_2. Domain D_0 is usually formed by many small domains and/or the interface between domains D_1 and D_2.

At the start of the simulation the perforated plates formed do not have any particular orientation, and, thus, D_0 occupies almost all of the simulation volume (not shown). However, at $18 \times 10^6\,\mathrm{fm}/c$ the system has formed two main domains, each occupying about 20% of the simulation volume. The domains are parallel plates with an hexagonal lattice of almost circular holes, the "waffle" phase discussed in Ref. [12]. All three domains have similar volumes from 20 to $40 \times 10^6\,\mathrm{fm}/c$, with neither dominating significantly over the other two. Furthermore, during this time there also little change in the average curvatures of the system, Fig. 3. However, the average energy per nucleon ϵ_i of each domain i follows a clear order, $\epsilon_2 < \epsilon_1 < \epsilon_0$. Although domain D_2 has a lower energy per nucleon than domain D_1, as domain

D_2 increases in volume its energy per nucleon ϵ_2 also increase, becoming similar to that of domain D_1. It is likely that if domain D_2 increased further in volume its average energy would become larger than that of domain D_1 and, thus, its growth is disfavored. Between 40 and 44×10^6 fm/c thermal fluctuations in the system force it to rearrange itself quickly. This is seen by abrupt changes in the volume and energy per nucleon of the three domains tracked. When this happens, domain D_2 decreases in volume until it almost disappears by the end of the run, $t = 55 \times 10^6$ fm/c. In the final configuration, domain D_1 occupies 70% of the simulation volume while domain D_0 (defects) occupy the remainder. It is likely that if this system is evolved for a longer time domain D_1 will occupy all of the simulation volume as is the case in smaller systems [13].
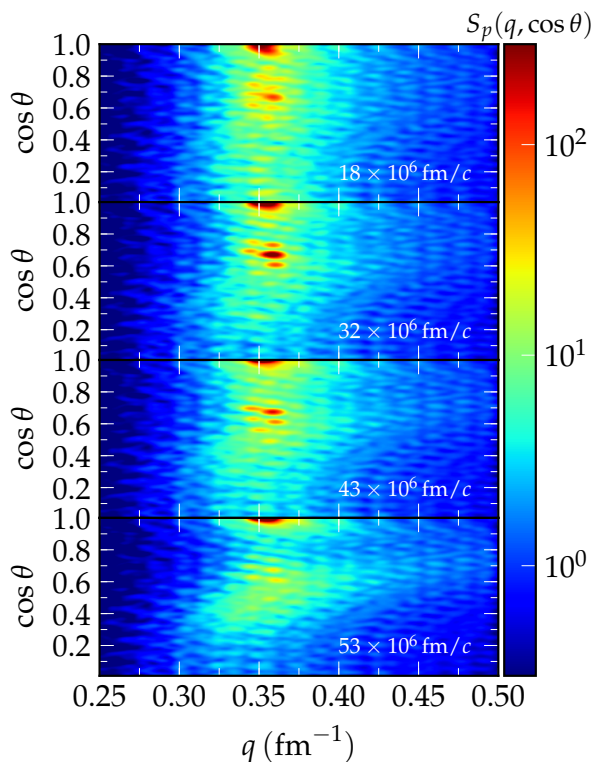
FIG. 6. (Color online) Proton structure factor $S_p(q, \cos\theta)$ for the 819 200 nucleon simulation as a function of the momentum transfer q and the angle θ between $\boldsymbol{q}$ and the direction where $S_p^e(\boldsymbol{q})$ is maximum, $\boldsymbol{q}_{\max} = \boldsymbol{q}_1$. This plot was generated from smoothing a 2D histogram of $S_p(q, \cos\theta)$ using a Gaussian filter with standard deviations $\sigma_q = 0.025$ fm^{-1} and $\sigma_{\cos\theta} = 0.05$.

In Figure 6 we plot the proton structure factor averaged over the azimuthal angle, $S_p(q, \cos\theta)$, at four different times in our simulation. For a clearer image we smooth the 2D histogram of $S_p(q, \cos\theta)$ using a Gaussian filter with standard deviations $\sigma_q = 0.025$ fm^{-1} and $\sigma_{\cos\theta} = 0.05$. We limit the plot to regions near $q \approx 0.35$ fm^{-1} which is where the first peak in the angle average $S_p(q)$ occurs, see Fig. 4. The angle $\theta(\boldsymbol{q})$ is chosen such that $\theta = 0$ ($\cos\theta = 1$) is parallel to the direction $\boldsymbol{q}_{\max}$ where $S_p^e(\boldsymbol{q}_{\max}) = \max(S_p^e(\boldsymbol{q}))$ in the last configuration of our simulation, i.e.,

$$\cos\theta(\boldsymbol{q}) = \frac{\boldsymbol{q} \cdot \boldsymbol{q}_{\max}}{|\boldsymbol{q}||\boldsymbol{q}_{\max}|}. \tag{8}$$

We note that the direction of $\boldsymbol{q}_{\max}$ coincides with $\boldsymbol{q}_1 = \frac{2\pi}{L}(-1, 2, 14)$, the direction we chose to define domain D_1, the largest one at the end of our simulation. Although this may seem obvious it is not always the case as discussed in Ref. [12] and for our 3 276 800 nucleons run discussed below.

The changes in domain sizes over time, seen in Fig. 5, can be inferred to a degree from the evolution of $S(q, \cos\theta)$ shown in Fig. 6. At 18×10^6 fm/c the system shows two prominent peaks in $S_p(q, \cos\theta)$: one at $\boldsymbol{q}_1 = \frac{2\pi}{L}(-1, 2, 14)$, $q \approx 0.35$ fm^{-1} and $\cos\theta = 1$, and another at $\boldsymbol{q}_2 = \frac{2\pi}{L}(-8, 9, 8)$, $q \approx 0.36$ fm^{-1} and $\cos\theta = 0.67$. This implies an angle $\theta_{12} \approx 48°$ between $\boldsymbol{q}_1$ and $\boldsymbol{q}_2$. As mentioned above, we used these two $\boldsymbol{q}_i$ to define domains D_1 and D_2. At this early time we see several other smaller peaks in $S_p(q, \cos\theta)$ in the range 0.34 fm$^{-1} \lesssim q \lesssim 0.37$ fm^{-1} and $0 \lesssim \cos\theta \lesssim 1$. Each peak corresponds to a direction perpendicular to a small domain, likely included in the defects domain D_0, while their magnitudes are correlated with the volume each of these small domains occupies.

In Figure 7 we show the configuration of the domains D_1, yellow plates, D_2, light blue plates, and D_0, red plates, at four different times in our simulation. At 18×10^6 fm/c the system is still dominated by the many small and likely uncorrelated domains that form D_0, Figs. 5 and 7. Between 18 and 32×10^6 fm/c both domains D_1 and D_2 increase in volume while D_0 decreases. This can be inferred by the darkening and sharpening of the peaks in $S_p(q, \cos\theta)$ near $\boldsymbol{q}_1$ and $\boldsymbol{q}_2$ at 32×10^6 fm/c, Fig. 6 and, even more clearly, in the second row of Fig. 7. Moreover, the number and magnitude of peaks in $S_p(q, \cos\theta)$ for $\cos\theta \leq 0.5$ decrease considerably when compared to the 18×10^6 fm/c configuration, meaning that domains nearly perpendicular to the D_1 are disfavored. After 43×10^6 fm/c in simulation time, domain D_2 decreases significantly in volume. This is accompanied by a decrease in magnitude of $S_p(q, \cos\theta)$ near $\boldsymbol{q}_2$ and in volume of the light blue region, see Fig. 7. However, around that same time, small domains nearly perpendicular to the domain D_1 have formed, as seen by the reappearance of many small peaks in the region $q \approx 0.35$ with $\cos\theta \lesssim 0.5$. Since we group these domains alongside others in D_0, domain D_0 increases in volume around that time, see Figs. 5 and 6 and red region in third row of Fig. 7. This change also correlates with a departure from average of the mean and Gaussian curvatures shown in Fig. 3. Nearly the end of our run, $t = 53 \times 10^6$ fm/c, domain D_2 has decreased to a very small volume which is separated from the domain D_1 by domain D_0. The near disappearance of domain D_2 and significant decrease in size of D_0 coincides with the disappearance, respectively,
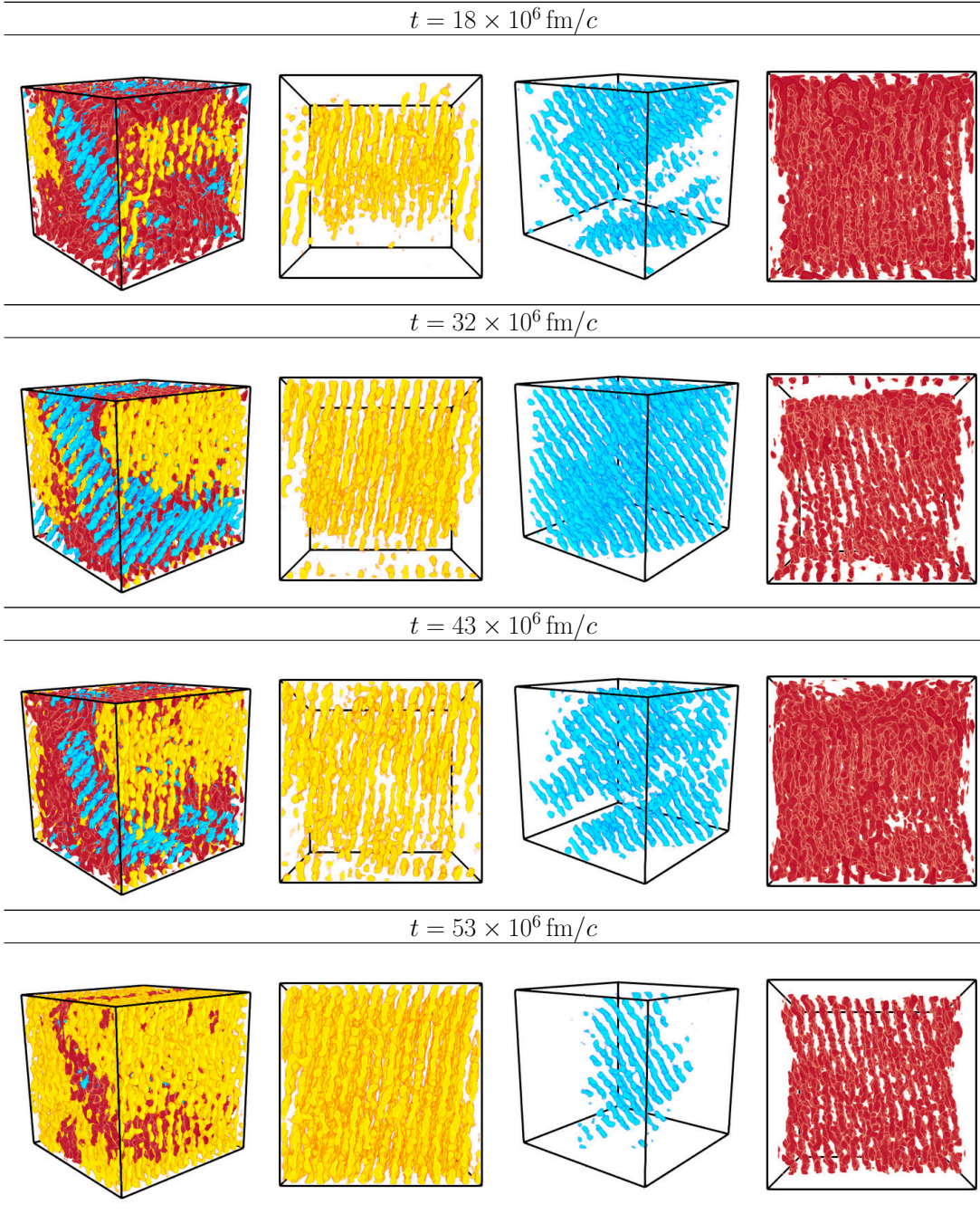
FIG. 7. (Color online) Configurations of our 819 200 nucleon run at four different times, $t = 18$, 32 43 and 53×10^6 fm/c. In the first column we show all domains: D_0 in red, D_1 in yellow, and D_2 in light blue. In columns 2, 3, and 4 we show, respectively, domains D_1, D_2 and D_0.

of the sharp peak in $S_p(q_2, \cos\theta_{12})$ and the decrease in the number and magnitude of peaks with $\cos\theta \lesssim 0.5$ near $q \approx 0.35$, bottom plot in Fig. 6.

2. Simulation with 1 638 400 nucleons

Our simulation run with 1 638 400 nucleons was equilibrated for 37×10^6 fm/c. This run cost approximately 3.2×10^5 node hours on the hybrid CPU/GPU nodes of the Titan supercomputer. Almost all of the nucleons arranged themselves in a single domain at the end of the run.
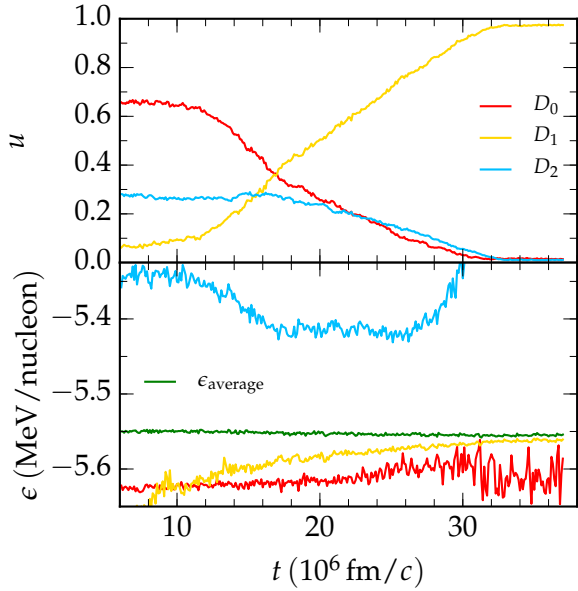
FIG. 8. (Color online) Volume fraction u (top) and potential energy per nucleon ϵ (bottom) for each domain in the system for the $1\,638\,400$ nucleon simulation as a function of simulation time. The three domains are D_0 (defects), D_1 ($\boldsymbol{q_1} = \frac{2\pi}{L}(-11, 11, 9)$), and D_2 ($\boldsymbol{q_2} = \frac{2\pi}{L}(-18, -1, 1)$). Green line in the bottom pane is the average system energy. We note that due to a system purge of Titan files and incomplete backup of our data configurations for the $819\,200$ nucleon run before $6 \times 10^6\,\mathrm{fm}/c$ were lost.
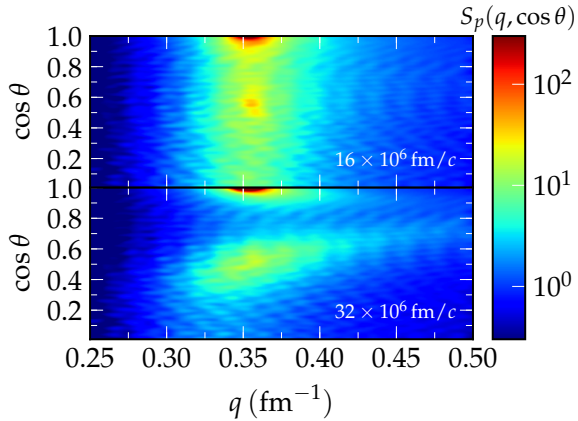
FIG. 9. (Color online) Similar to Fig. 6 but for the $1\,638\,400$ nucleon system at times $t = 16$ and $32 \times 10^6\,\mathrm{fm}/c$.

We perform a data analysis like the one described for the $819\,200$ nucleon system. By computing $S(\boldsymbol{q})$ halfway through the simulation we identify two dominant domains: D_1 defined by $\boldsymbol{q_1} = \frac{2\pi}{L}(-11, 11, 9)$ and D_2 defined by $\boldsymbol{q_2} = \frac{2\pi}{L}(-18, -1, 1)$. Here $L = 320\,\mathrm{fm}$. Similarly to the $819\,200$ case, the angle between the two domains is $\approx 53°$. Again we define D_0 as the set of nucleons that belong to neither D_1 or D_2.

From the data we have we observe that domain D_2 quickly grows in size and at $6 \times 10^6\,\mathrm{fm}/c$ already occupies 30% of the simulation volume, top panel of Fig. 8. However, this domain has a significantly larger energy per nucleon than domain D_1, bottom panel of Fig. 8. Thus, the latter is favored and quickly grows: by the end of the run both D_0 and D_2 have almost completely disappeared, while D_1 occupies almost all of the simulation volume. This progression can also be inferred from the evolution of the peaks in $S_p(q, \cos\theta)$, plotted in Fig. 9, and explicitly shown in Fig. 10.

3. Simulation with $3\,276\,800$ nucleons

The simulation with $3\,276\,800$ nucleons is the largest one in our work and, to our knowledge, the largest nuclear pasta simulation performed to date. This run was performed exclusively on the hybrid CPU/GPU nodes of the Big Red 2 supercomputer and cost approximately 1.9×10^6 node hours. Despite its long run time, this systems is still composed of several domains in its final configuration at $t = 32 \times 10^6\,\mathrm{fm}/c$.

In Fig. 11 we plot the volume fraction u and potential energy per nucleon ϵ for seven domains. These domains are

1. D_1 defined by $\boldsymbol{q_1} = \frac{2\pi}{L}(-10, 19, 7)$,

2. D_2 defined by $\boldsymbol{q_2} = \frac{2\pi}{L}(-11, 13, 15)$,

3. D_3 defined by $\boldsymbol{q_3} = \frac{2\pi}{L}(-4, 8, 21)$,

4. D_4 defined by $\boldsymbol{q_4} = \frac{2\pi}{L}(-14, 15, 10)$,

5. D_5 defined by $\boldsymbol{q_5} = \frac{2\pi}{L}(-16, 8, 14)$,

6. D_6 defined by $\boldsymbol{q_6} = \frac{2\pi}{L}(-13, 18, -5)$,

7. D_0 defined by nucleons that are not in D_i, $i = 1, \ldots, 6$.

Here $L = 403\,\mathrm{fm}$ is the length of the box. We chose the domains ordered by the values of $S^e(\boldsymbol{q})$ in the final configuration omitting angles within $15°$ of $\boldsymbol{q_i}$, $i = 1, \ldots, 6$. We notice that domain D_1 does not coincide with the domain which occupies the largest volume by the end of the simulation, which is domain D_2. This may be due to nucleons in domain D_1 having less deviation from their average position than nucleons in domain D_2.

From the structure factor plot, Fig. 12, we also see that this simulation has multiple large domains at the end of the run. This is clear from the existence of a large area with $S_p(q, \cos\theta) \gtrsim 10^2$ around $q \approx 0.35\,\mathrm{fm}^{-1}$ instead of one or two localized peaks like in the smaller simulations. Over time the magnitude of $S_p(q, \cos\theta)$ increases for $q \approx 0.35\,\mathrm{fm}^{-1}$ and $\cos\theta \gtrsim 0.6$ while decreasing for $\cos\theta \lesssim 0.6$. This follows from the defect domain D_0, which includes small domains that form an angle $\theta \gtrsim 45°$ with respect to domain D_1, decreasing from 40% in volume to 15% from $t = 16$ to $t = 32 \times 10^6\,\mathrm{fm}/c$.
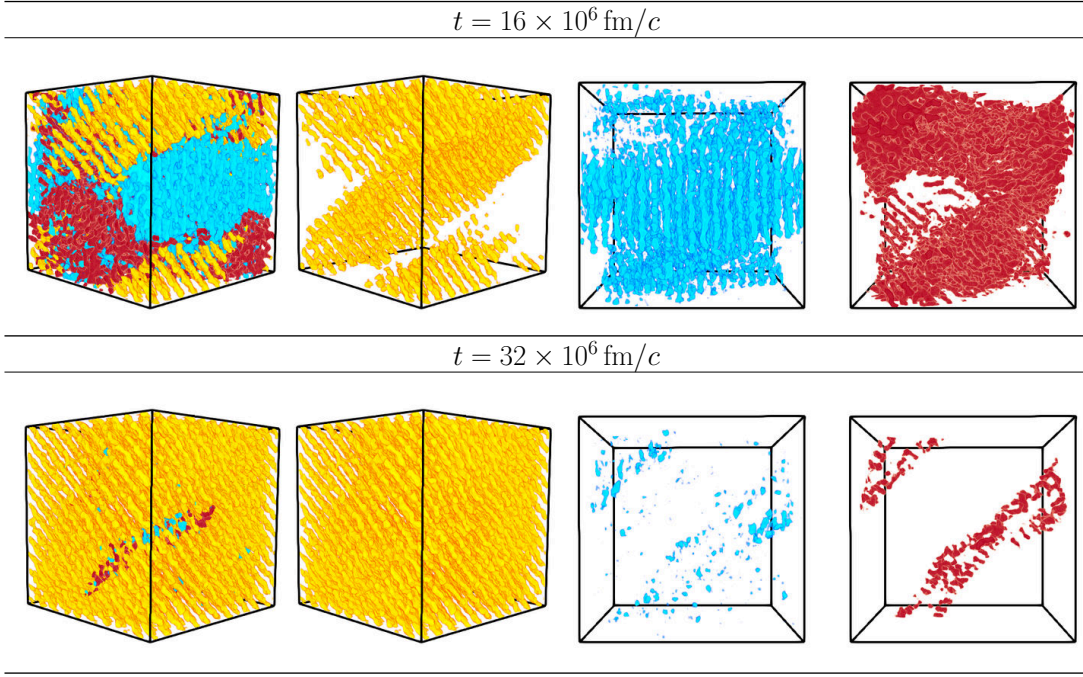
$$t = 16 \times 10^6 \, \mathrm{fm}/c$$

$$t = 32 \times 10^6 \, \mathrm{fm}/c$$

FIG. 10. (Color online) Similar to Fig. 7 but for the $1\,638\,400$ nucleon system at times $t = 16$ and $32 \times 10^6 \, \mathrm{fm}/c$.
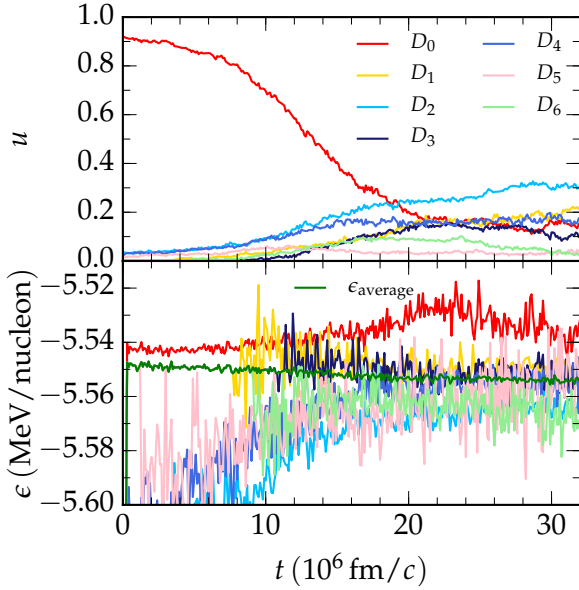

FIG. 11. Volume fraction u (top) and potential energy per nucleon ϵ (bottom) for each domain in the system for the $3\,276\,800$ nucleon simulation as a function of simulation time. The seven domains are D_0 (defects), D_1 ($\boldsymbol{q}_1 = \frac{2\pi}{L}(-10, 19, 7)$), D_2 ($\boldsymbol{q}_2 = \frac{2\pi}{L}(-11, 13, 15)$), D_3 ($\boldsymbol{q}_3 = \frac{2\pi}{L}(-4, 8, 21)$), D_4 ($\boldsymbol{q}_4 = \frac{2\pi}{L}(-14, 15, 10)$), D_5 ($\boldsymbol{q}_5 = \frac{2\pi}{L}(-16, 8, 14)$), and D_6 ($\boldsymbol{q}_6 = \frac{2\pi}{L}(-13, 18, -5)$). Green line in the bottom pane is the average system energy. To reduce noise in the plot of ϵ we do not show the values for domains at times when their volume fraction is $u < 0.02$.

The matrix of the angles between the 6 largest domains
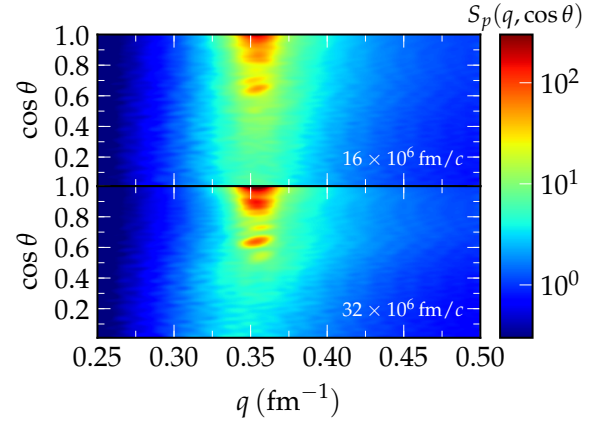
FIG. 12. (Color online) Similar to Fig. 6 but for the $3\,276\,800$ nucleon system at times $t = 16$ and $32 \times 10^6 \, \mathrm{fm}/c$.

(all domains chosen not including the ones that make up D_0) is given by

$$\frac{\boldsymbol{q}_i \cdot \boldsymbol{q}_j}{|\boldsymbol{q}_i||\boldsymbol{q}_j|} = \begin{pmatrix} 0.0° & 25.6° & 48.9° & 16.2° & 36.9° & 31.8° \\ 25.6° & 0.0° & 26.6° & 15.6° & 18.1° & 54.2° \\ 48.9° & 26.6° & 0.0° & 42.2° & 35.5° & 79.9° \\ 16.2° & 15.6° & 42.2° & 0.0° & 21.0° & 39.3° \\ 36.9° & 18.1° & 35.5° & 21.0° & 0.0° & 56.9° \\ 31.8° & 54.2° & 79.9° & 39.3° & 56.9° & 0.0° \end{pmatrix}.$$

$$(9)$$

As observed for the two main domains in the smaller simulations, the system is dominated by domains that form angles $\theta \lesssim 45°$ with each other. Only domain D_6 is consistently found at angles $\theta \gtrsim 45°$ with respect to

other domains. As shown in Figs. 11 and 13, it has a volume similar to domain D_1 halfway through the simulation but almost disappears by the end of the run. This seems to indicate that for the "waffle" phase domains nearly perpendicular to other ones disappear first, likely due to the large energy that need to be stored in its interface with other domains. The defects domain D_0 also decreases considerably in volume by the end of the run when compared to the halfway point. Most of its volume was absorbed by the domains D_i, $i = 1, \ldots, 4$.

Due to the high computational cost of this run we do not evolve it any further. Based on the results for the other simulations we speculate that if run for longer all domains in this simulation will eventually converge to a single one. It is unclear, though, which one of the four larger domains at the end of the run would prevail over the others or if any other domains would appear.

At this point it may be appropriate to speculate on the likely grain (or domain) size in the NS crust. Unfortunately, almost nothing is known. One possibility is that the grain size is set by multiplying a domain growth rate, that we may be able to approximately observe in our simulations, with a time for new crust formation. This formation time might be set by the rate of crust cooling, in an isolated newly born star, or by the accretion rate as material is compressed to higher densities where it forms a new pasta phase.

B. Simulations with $Y_p = 0.40$

We examine simulations of seven different sizes for MD simulations with proton fraction $Y_p = 0.40$. Five runs were already discussed in Ref. [13]; the ones containing 51 200, 76 800, 102 400, 204 800, and 409 600 nucleons that were evolved at $n = 0.05 \, \text{fm}^{-3}$ at $T = 1 \, \text{MeV}$ for at least $10 \times 10^6 \, \text{fm}/c$. The run with 409 600 nucleons was evolved for a further $3 \times 10^6 \, \text{fm}/c$ for this work as its defects were not fully equilibrated. This has little effect on our estimate for the impurity parameter Q_{imp} of the pasta, our main result in Ref. [13]. We include two additional runs: a small one with 61 440 nucleons and a large one with 819 200 nucleons. If let to evolve without the influence of any external potentials all of these systems form plates connected by Terasaki ramps [11, 13, 95–97]. A summary of these runs is discussed in Table II.

We also perform runs of the same seven sizes acted upon by an external sinusoidal potential following Ref. [13]. The external potential is removed after a short time, $0.1 \times 10^6 \, \text{fm}/c$, and the runs are left to equilibrate for another $2.9 \times 10^6 \, \text{fm}/c$. Due to the initial influence of the external potential, parallel plates form. In all cases, the parallel plates are only stable for runs with the number of plates detailed in Tab. III. When trying to create a different number of parallel plates within the simulation volume the plates quickly became unstable after the removal of the external potential and merge to form defects. We did not study the topology evolution of runs where

TABLE II. Summary of our MD runs with proton fraction $Y_p = 0.40$. We list the number of nucleons in the first column, the total evolution time in the second column and the side of the simulation box in the third column. In the fourth and fifth columns we enumerate, respectively, the number of left-handed and right-handed Terasaki ramps. In the sixth column we describe the ramps configuration, see text and Fig. 21.

Nucleons	t_{total} (10^6 fm/c)	L_{box} (fm)	Left	Right	Configuration
51 200	10.0	100.8	4	4	dipole
61 440	13.5	107.1	4	4	dipole
76 800	14.5	115.4	2	0	isolated
102 400	12.0	127.0	4	4	dipole
204 800	18.0	160.0	1	1	dipole
409 600	17.0	201.6	1	1	dipole
819 200	18.0	254.0	1	1	dipole

unstable parallel plates merged after a short simulation time, even though that may be an interesting problem on its own.

TABLE III. Number of plates N_p and distance d between the center of neighboring plates for simulations of different sizes. Runs marked with a † were performed for a previous work [13] while ‡ denotes new runs.

Nucleons	N_p	d (fm)
51 200†	6	16.8
61 440‡	6	17.9
76 800†	7	16.5
102 400†	7	18.1
204 800†	10	16.0
409 600†	11	18.3
812 900‡	14	18.1

In Fig. 14 we show the normalized mean curvature and normalized Gaussian curvatures for the $Y_p = 0.40$ simulations [12, 50]. The four smaller runs seemingly converged to a stable configuration within $3 \times 10^6 \, \text{fm}/c$, while the larger ones took four to five times longer. Note that the 51 200, 409 600, and 819 200 nucleon systems with $Y_p = 0.40$ have equilibrated in, respectively, 2, 15, and $9 \times 10^6 \, \text{fm}/c$. These time scales are significantly faster than the convergence time for $Y_p = 0.30$ runs of the same size. This is valuable as the computational cost of a run scales with $\mathcal{O}(N^2 Y_p^2)$. Furthermore, the three larger simulations have very similar curvatures at the end of the runs, while the four smaller ones do not seem to obey any clear trend with respect to their size. As we will show below this is due to the types of defects formed in each of the runs.

Similarly to the $Y_p = 0.30$ case we use our algorithm of Sec. II C to separate the system in different domains. In the $Y_p = 0.40$ cases, however, we only analyze two domains. Domain D_1 is defined by protons with structure factor $S_j^e(\boldsymbol{q}_{\text{max}}, t_f) > 0.40$, see Eq. (5). Here $\boldsymbol{q}_{\text{max}}$ is the most common normal to the plates formed in each system

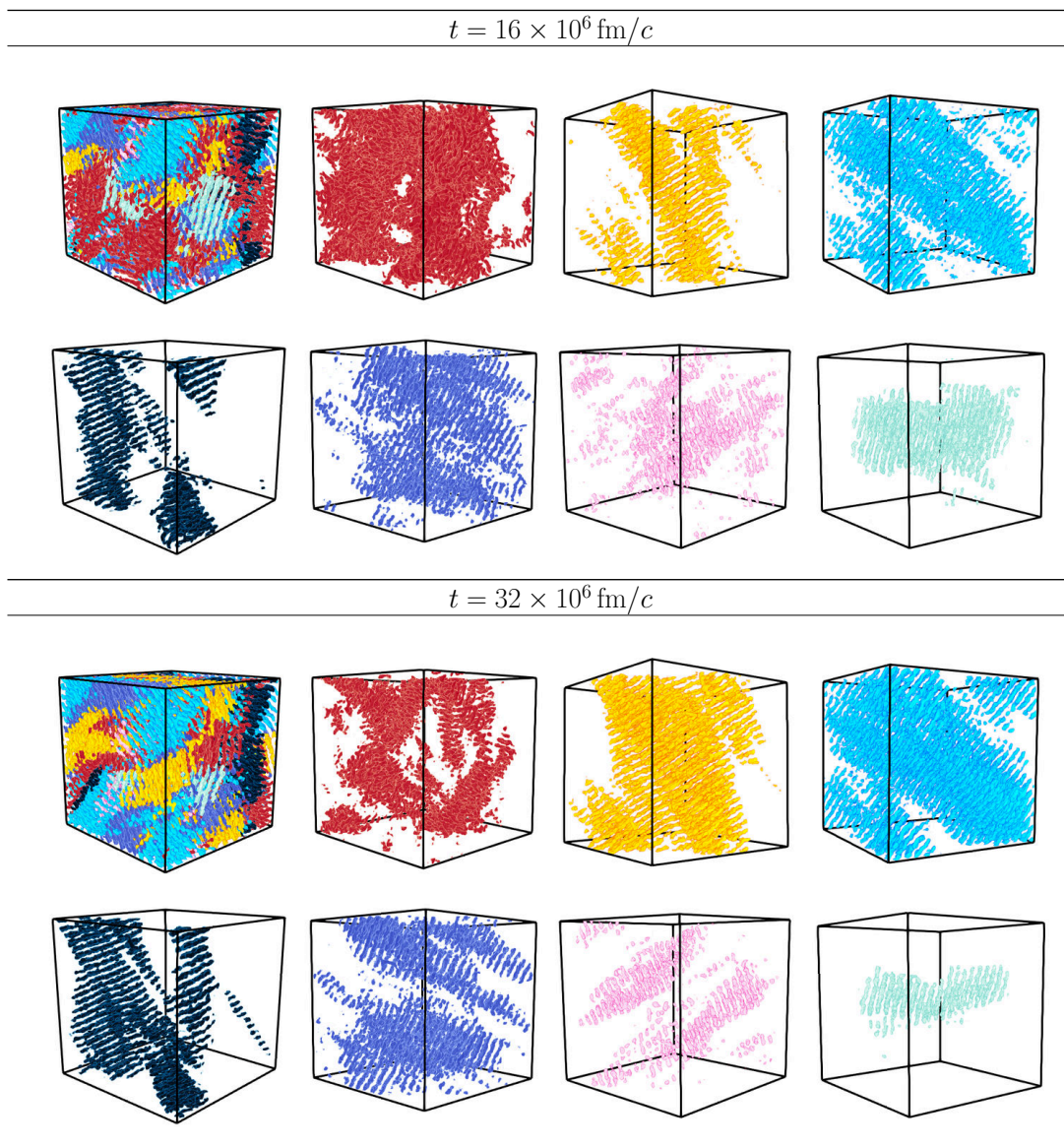FIG. 13. (Color online) Configuration of our $3\,276\,800$ nucleon simulation at two different times, $t = 16 \times 10^6\,\mathrm{fm}/c$ and $t = 32 \times 10^6\,\mathrm{fm}/c$. We show seven different domains: D_0 (red), D_1 (yellow), D_2 (light blue), D_3 (black), D_4 (dark blue), D_5 (pink), and D_6 (light green). In the top row of each time we show from left to right all domains in the system followed by domains D_0, D_1, and D_2. In the bottom row from left to right we show domains D_3, D_4, D_5, and D_6.

and obtained from the highest peak in $S(\boldsymbol{q})$, shown in Fig. 16. Protons which do not belong to domain D_1 are set as part of domain D_0.

In the top panel of Fig. 15 we plot the volume fraction u_0 of nucleons in domain D_0 (top) for the runs with defects. The volume occupied by domain D_1 is $u_1 = 1 - u_0$. The three larger simulations have, at the end of their run, a very similar volume fraction of defects, alluding that topology and defect density may have converged for the larger runs. As in the curvature case, the smaller runs do not show any clear trend with respect to their size. However, the absolute value of curvatures do seem correlated amongst themselves and with the volume fraction

u_0 occupied by the defects domain D_0.

In the bottom panel of Fig. 15 we plot the energy per nucleon ϵ of the systems with defects and compare with the systems forced to form parallel plates perpendicular to one of the sides of the box by an external potential. For most simulation sizes the energy per nucleon is lower for systems that have defects instead of parallel plates. The exceptions are the runs with $61\,440$ that has a larger energy per nucleon in the system with defects, and the runs with $102\,400$, and $409\,600$, where the energies are almost the same in both cases. Ideally, we expect a system with parallel plates to have smaller energy per particle than one with defects. Our results showing that this is
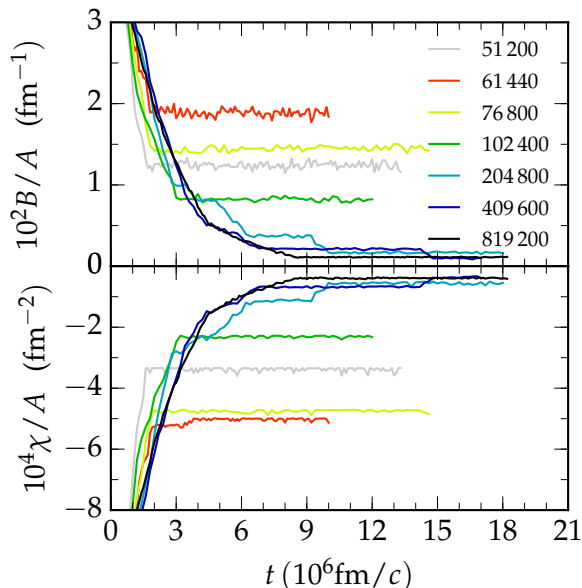
FIG. 14. (Color online) Plots of the normalized mean curvature B/A (top) and normalized mean Gaussian curvature χ/A (bottom) as a function of simulation time t for seven simulations with $Y_p = 0.40$, $n = 0.050\,\text{fm}^{-3}$ and $T = 1.0$ MeV.
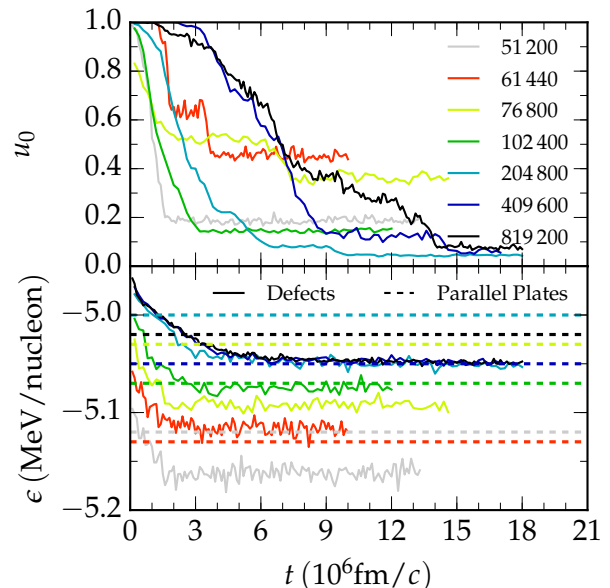
FIG. 15. (Color online) Volume fraction u_0 of nucleons in domain D_0 (top) and potential energy per nucleon ϵ (bottom). Domain D_0 is formed by defects while D_1 defined by parallel plates perpendicular to $\boldsymbol{q}_1 = \boldsymbol{q}_{\text{max}}$, see text. Except for the 76 800 run domain D_1 is formed exclusively by parallel plates, and thus u_0 is the volume of defects.

often not the case for our simulations is a consequence of finite size effects of the systems studied. Slow expansion runs with up to 102 400 nucleons similar to the ones of Schneider *et al.* [50] show that parallel plates tilted with respect to the sides of the box can form at $n = 0.05\,\text{fm}^{-3}$. These tilted plates have lower energies per particle than the ones obtained for either the run with defects and the ones with parallel plates discussed here.

In Fig. 16 we show the angle average structure factor for protons $S_p(q)$ for our seven simulations as well as their upper and lower bounds, defined by the maxima and the minima in $S_p(\boldsymbol{q})$ for a given $q = |\boldsymbol{q}|$. All structure factors have a similar qualitative behavior, with sharp peaks at $q' \approx 0.34\,\text{fm}^{-1}$ and $2q'$. The quantitative behavior, on the other hand, only seems to agree for the three larger simulations as the four smaller ones have a few other minor peaks between q' and $2q'$ that don't appear in the larger ones. As we will show next, this is due to the different structures of the defects formed within the simulation volume.

The topology of the defects formed can be inferred from Fig. 17, where we plot the structure factors $S_p(q, \cos\theta)$ with respect to the direction of $\boldsymbol{q}_{\text{max}}$ where $S_p^e(\boldsymbol{q})$ is a maximum. As in Sec. III A we histogram the values of $S_p(q, \cos\theta)$ and smooth it with a Gaussian filter. For better visualization we use standard deviations $\sigma_q = 0.025\,\text{fm}^{-1}$ and $\sigma_{\cos\theta} = 0.05$ in the Gaussian filter for simulations with 204 800 and larger and $\sigma_q = 0.033\,\text{fm}^{-1}$ and $\sigma_{\cos\theta} = 0.067$ for simulations with 102 400 nucleons or smaller. In the $S_p(q, \cos\theta)$ plots the main domain appears as a peak with $q \approx 0.34\,\text{fm}^{-1}$ and

$\cos\theta \approx 1$. Secondary domains appear as peaks with $q \approx 0.34\,\text{fm}^{-1}$ and $\cos\theta < 0.9$. It is clear from these plots that the types of defects is different between the runs. Because of how peculiar the structure formed in the 76 800 nucleon run is, some regions with $q \lesssim 0.25\,\text{fm}^{-1}$ in its plot of $S_p(q, \cos\theta)$, third row of Fig. 17, are not covered by any combination of q and $\cos\theta$. These are seen as white pixels in the plot. Widening the parameters of the Gaussian filter would remove those at the expense of further blurring out the peaks near $q = 0.35\,\text{fm}^{-1}$.

In Fig. 21 we show the final configurations for the $Y_p = 0.40$ systems separated as two domains: D_0, defects, and D_1, defined by the maximum in $S(\boldsymbol{q})$. With the exception of the 76 800 nucleons simulation, domain D_1 is always formed by parallel plates.

In the 51 200 nucleon system the normal to the plates and normal to the defects form an angle of about 45° with respect to each other. This is clear from the location of the second maxima in $S_p(q, \cos\theta)$ at $q \approx 0.34\,\text{fm}^{-1}$ and $\cos\theta \approx 0.70$ ($\theta \approx 40°$) seen in Fig. 17. This is also clear from the configurations shown in the top row of Fig. 21. The pattern of Terasaki ramps forms a dipole with eight helical ramps side by side, four left-handed and four right-handed helices, which connect the five parallel plates within the simulation volume. This is the dipole pattern discussed in Refs. [96, 97]. In Fig. 18 we show a schematic picture of the defects since our domain detection algorithm does not clearly separate part of the helices from the planes in this case.
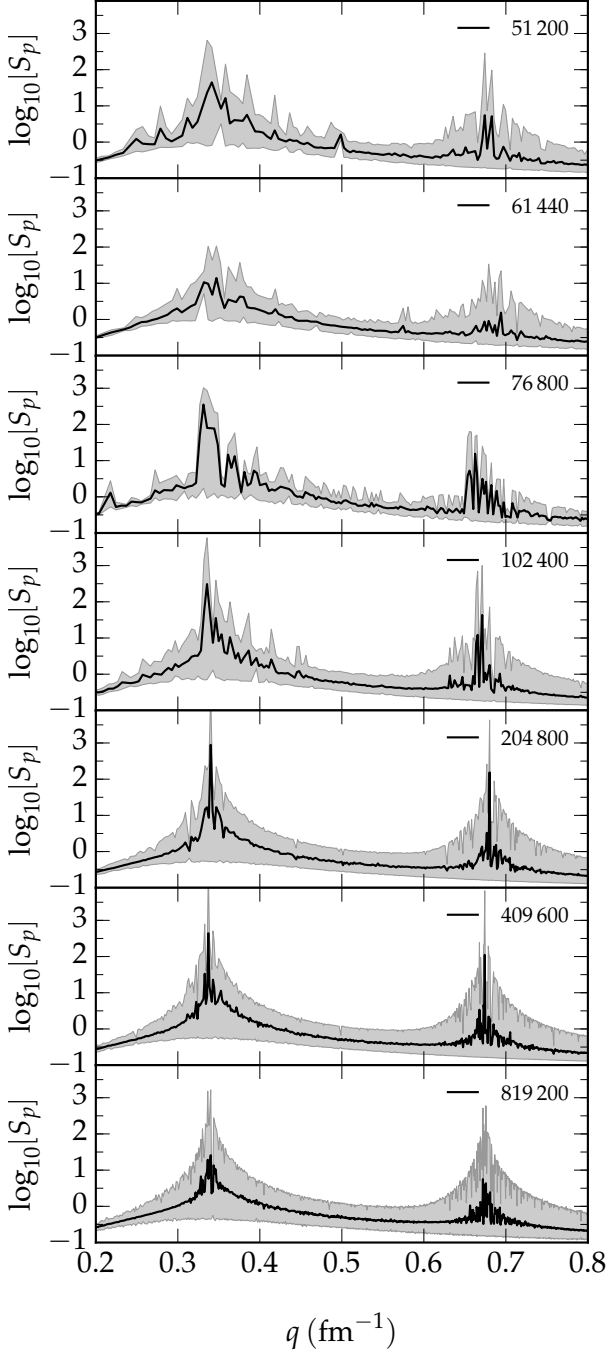
Similarly to the 51 200 simulation, the 61 440 nucleon

FIG. 16. Plots of the angle averaged proton structure factor $S_p(q) = \langle S_p(\boldsymbol{q}) \rangle_q$ (thick black lines) for the last 1.0×10^6 fm/c of each simulation run. The average is bounded by the maximum and minimum in $S_p(q)$ for each $q = |\boldsymbol{q}|$ (shaded grey area).
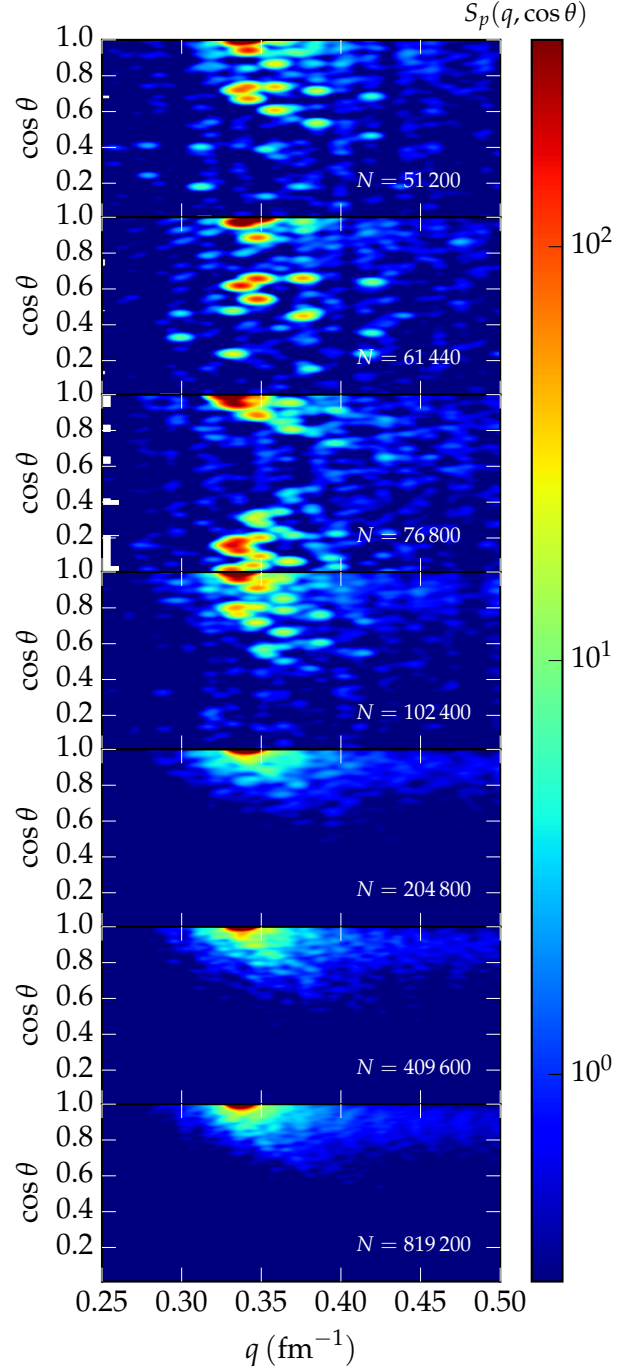
FIG. 17. Azimuthal average $S_p(q, \cos\theta)$ of the proton structure factor for the last 1.0×10^6 fm/c of each run. The angle θ is defined in Eq. (8).

run also forms a set of eight helices with the pattern scheme shown in Fig. 18, see second row of Fig. 21. The main difference here is that in this simulation the helices form in a different angle with the sides of our simulation

box. In the 61 440 nucleon case our domain algorithm performs better than in the 51 200 nucleon case and, thus, the volume fraction u_0 of domain D_0 appears to be twice the size in the slightly larger run as more protons are identified as belonging to domain D_0, see top panel of Fig. 15.

are at an angle of approximately 45° with each other, Fig. 17. However, the magnitude of the second peak in the 102 400 nucleon system is smaller than in the 51 200 nucleon system, fourth row in Fig. 21, because in the larger system the defects occupy, proportionally, a smaller volume, see plot of u_0 in Fig. 15.
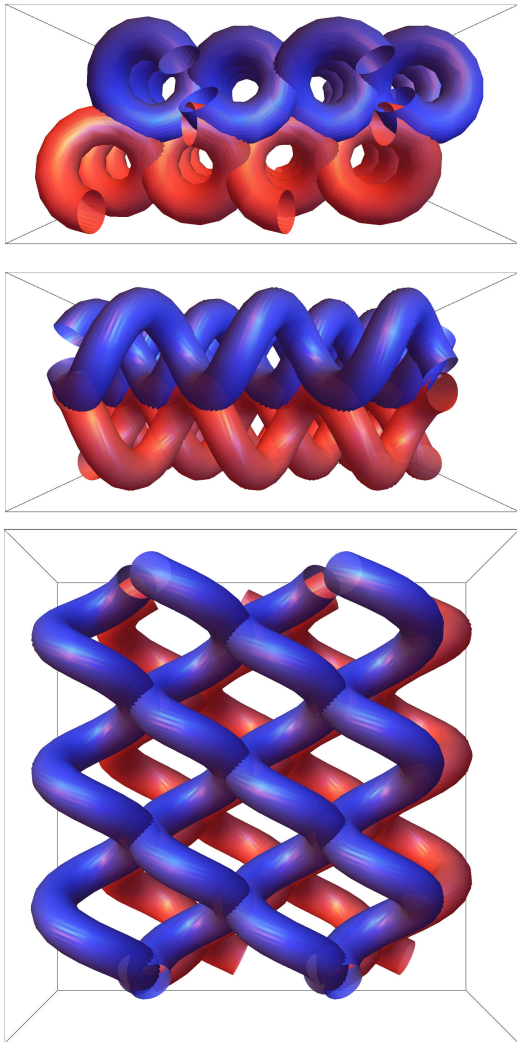

FIG. 18. Schematic top (top panel) and side views (center and bottom panels) of the dipole pattern formed by eight helical ramps. In red (blue) we show the right (left) -handed helices. In the bottom panel we can identify the position of the planes that would form a 45° angle with respect to the helices and connect the helices.
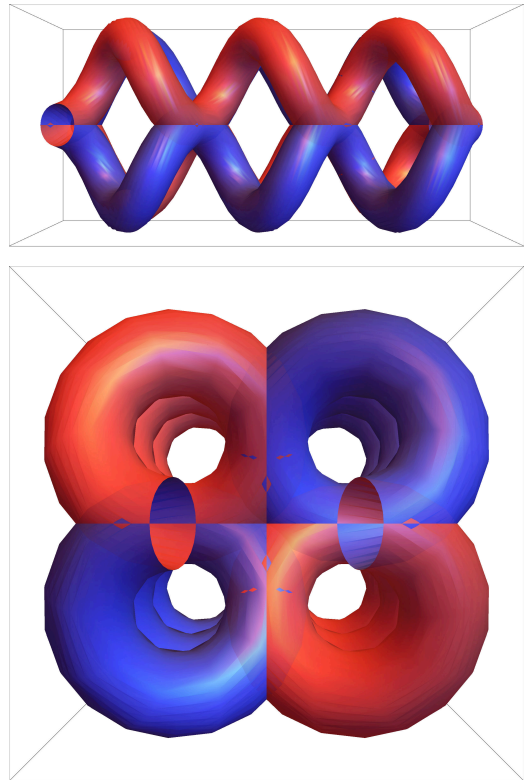

FIG. 19. Schematic side (top panel) and top views (bottom panel) of one of the quadrupole possibilities formed by four helical ramps. In red (blue) we show the right (left) -handed helices.

The topology formed by the 76 800 nucleon system is somewhat different than what we see in all other simulations. Here two sets of plates that are almost perpendicular to each other compete, with neither occupying significantly more than half of the simulation volume by the end of the run. This is seen by the location and magnitude of the second largest peak in $S_p(q, \cos\theta)$ which occurs at $q \approx 0.33\,\mathrm{fm}^{-1}$ and $\cos\theta \lesssim 0.2$ ($\theta \gtrsim 78°$), Fig. 17. This system is even more peculiar in that it formed two helical ramps perpendicular to each other, both of which are left-handed, see third row of Fig. 21. This is unlike any of the other systems we have simulated where right- and left-handed ramps appear in equal numbers.

The 102 400 nucleon system is very similar to the 51 200 and 61 440 systems: the helical ramps and plates

The three larger systems, with 204 800, 409 600, and 819 200 nucleons, have a similar evolution history. Before achieving their final configuration, the three systems go through similar stages to the ones described by Berry *et al.* [97] and shown in their Fig. 1. However, due to the larger size of the simulations presented here, the system forms several "ramps" connecting its planes. Over time, ramps move towards each other and the ones with same helicity merge while pairs with opposite helicities persist. Pairs of ramps also attract each other as the system evolves. At this point, we speculate that two events can take place. The angle of approach of the pairs of helices can be such that it forms a quadrupole as the one schematically shown in Fig. 19. This configure is stable and the system, likely, does not evolve further. This is what is observed by Berry *et al.* in their 75 000 nucleon simulation [97]. In the large runs discussed here, however, the pairs of ramps approach each other in such a way that ramps with the same helicity face each other. As this happens, thermal fluctuations in the system cause
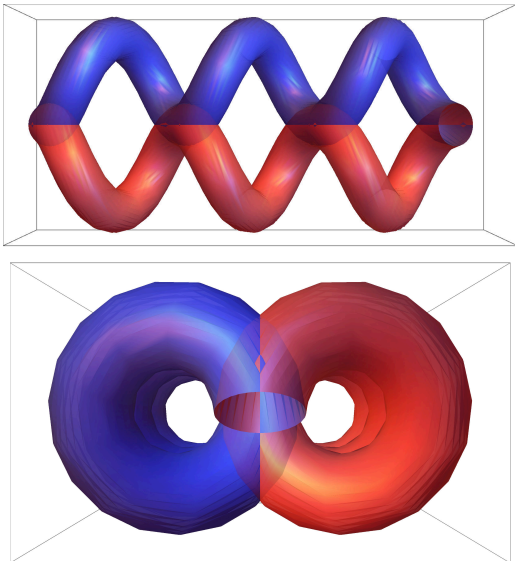
FIG. 20. Schematic side (top panel) and top views (bottom panel) of one of the dipole possibilities formed by two helical ramps. In red (blue) we show the right (left) -handed helices.

ramps with same helicity to merge and a dipole as the one shown in Fig. 20 is created. Unlike the dipole configurations observed in the smaller runs, where helices and plates are at a 45° with each other, in the large runs the helices are at a 90° angle with the plates. This is also noticed by a lack of a second significant peak in $S_p(q, \cos\theta)$ in Fig. 17.

Although both the curvatures and the structure factors in the $Y_p = 0.40$ runs seem to have converged as the simulation size was increased it is unclear whether this convergence would remain true if larger systems were simulated. Furthermore, we observed three different types of defects in these simulations in the six runs performed. And yet another type was observed by Berry *et al.* [97] in similar MD simulations. Presently, there is no clear way of knowing whether this would remain true if we simply repeated simulations for systems of the same size or if we performed even larger simulations. Thus, further studies of these phases are warranted.

IV. CONCLUSIONS

Numerical simulations of nuclear pasta have attracted attention lately as we have finally reached a stage where efforts to find indirect evidence of its existence are underway. Nuclear matter properties at sub-saturation densities, where the pasta phases are likely to form, can be constrained from the cooling curves of accreting neutron stars in quiescence [36–40] and from LIGO-Virgo combined searches for r-mode gravitational waves signals from spinning down neutron stars [11, 32, 35, 109]. It may also be the case that the neutrino signal from a galactic supernovae or a neutron star merger will shed
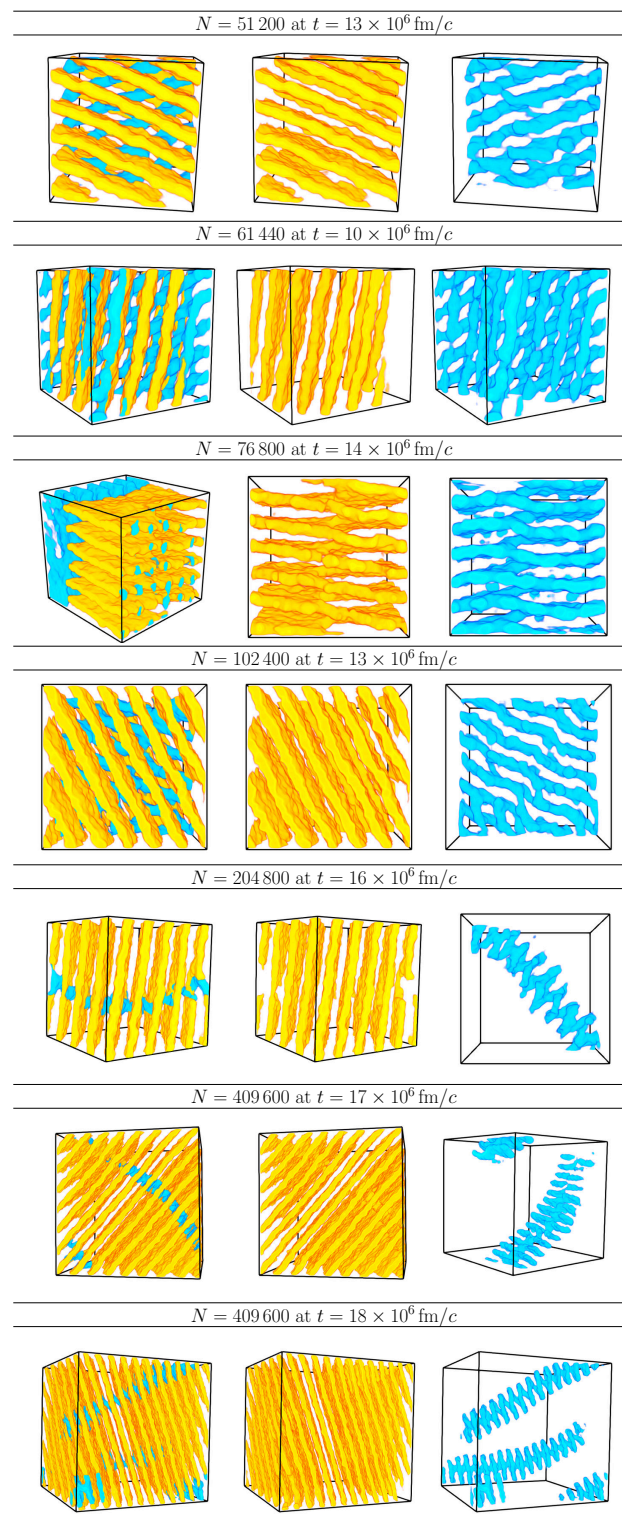

FIG. 21. (Color online) Last configuration of each of out $Y_p = 0.40$ runs. For each system we show two different domains, D_0 (light blue) and D_1 (yellow).

light on the formation and properties of nuclear pasta [26, 27]. Some of the pasta properties and its effects on

physical observables are a function of the nucleon structure factors [7, 8], which can be computed from numerical simulations. However, finite-size effects and computational limitations are a substantial problem that should be overcome in order to accurately determine nuclear pasta observables [13].

In this work we studied, to our knowledge, the largest nuclear pasta systems to date where nucleonic degrees of freedom are taken into account. Using the IUMD code and Big Red 2 and Titan computer resources we simulated nuclear pasta systems with up to 3 276 800 nucleons for proton fractions $Y_p = 0.30$ and with up to 819 200 nucleons for $Y_p = 0.40$.

All $Y_p = 0.30$ runs formed the expected "waffle phase" [50, 55]. We analyzed the structure factor dependence on simulation size and showed that there is qualitative agreement between the results obtained for simulations with 51 200 up to 3 276 800 nucleons. However, there are some quantitative differences in the results for simulations of such different sizes which are an artifact of the finite-size of the systems studied. Our results show that simulations with less than a hundred thousand nucleons still suffer from significant finite-size effects that need to be accurately addressed when predicting the transport properties of nuclear pasta, at least for the topologies studied in our work. Nonetheless, it is encouraging that there is a good agreement for the structure factor main peak location and its magnitude from much smaller simulations using a different method [14]. Besides quantification of finite size effects, we introduced an algorithm that analyzes the evolution of domains within the simulations to test their formation and equilibration time-scales beyond what is possible by computing Minkowski functionals alone. We noticed that most of our $Y_p = 0.30$ runs, if left to equilibrate for enough time, formed a single domain within the simulation volume. The exception being the largest of our runs, with 3 276 800 nucleons, which still had six large domains and many defects by the time we stopped evolving it due to its very high computational cost. The high cost of MD computations stemming from long range Coulomb repulsion between protons can be decreased with the implementation of robust fast multipole method algorithm for Yukawa-type potentials [100–102]. Excluding significant advances in computer performance, this may be the only way to simulate nuclear pasta systems beyond a few million nucleons that need to be evolved for tens of millions of times steps in order to reach equilibrium.

We also performed a few MD simulations with proton fraction $Y_p = 0.40$. These runs, unless acted upon an external potential, formed parallel plates connected by "Terasaki" ramps [11, 13, 95–97]. For same size simulations, the $Y_p = 0.40$ runs equilibrated significantly faster than their $Y_p = 0.30$ counterparts. We found that the set of planes and Terasaki ramps formed different topologies that depended on simulation size. Amongst the topologies formed we observed dipoles composed of groups of eight parallel helical ramps, four left-handed and four

right-handed, at an angle of 45° with the planes in three of our small simulations, the ones with 51 200, 61 440, and 102 400 nucleon runs. The three largest runs, in their final configuration, formed only one pair of parallel helical ramps, one left-handed and one right-handed. These ramps had a propensity to attract each other and form a dipole configuration at an angle of 90° with respect to the parallel planes. Finally, the simulation with 76 800 nucleons was unique in that it formed two left-handed helices, and no right-handed ones. These helices were at 90° with respect to each other and with respect to the the planes they connected. We did not observe any quadrupole setup of helical ramps as seen by Berry *et al.* in Ref. [97] for a system with 75 000 nucleons. This may indicate that simulations with $\lesssim 102 400$ nucleons may be considerably sensitive to their size and the initial conditions of the simulation.

From the self-assembled patterns seen in our simulations and the time to establish and equilibrate them we estimate that, in order to minimize finite size-effects in computations of transport properties of nuclear pasta, it may be necessary to perform simulations with hundreds of thousands of nucleons. This is discouraging from the point of view of computational costs as simulations this large are unlikely to be possible anytime soon for full quantum-mechanical calculations [55, 63]. However, by understanding how finite-size effects affect the results for structure factor of nucleons and the transport properties of nuclear pasta we can make informed guesses about the direction which results should be corrected for smaller simulations, such as the ones shown here and by compilations of the results of Nandi and Schramm [14]

[1] R. Nandkumar and C. J. Pethick, Mon. Not. Royal Astron. Soc. **209**, 511 (1984).
[2] A. Chugunov and D. Yakovlev, Astron. Rep. **49**, 724 (2005).
[3] D. G. Ravenhall, C. J. Pethick, and J. R. Wilson, Phys. Rev. Lett. **50**, 2066 (1983).
[4] M. aki Hashimoto, H. Seki, and M. Yamada, Progress of Theoretical Physics **71**, 320 (1984).
[5] K. Oyamatsu, M. Hashimoto, and M. Yamada, Progress of Theoretical Physics **72**, 373 (1984).
[6] R. Williams and S. Koonin, Nuclear Physics A **435**, 844 (1985).
[7] C. J. Horowitz, M. A. Pérez-García, and J. Piekarewicz, Phys. Rev. C **69**, 045804 (2004).
[8] C. J. Horowitz, M. A. Pérez-García, J. Carriere, D. K. Berry, and J. Piekarewicz, Phys. Rev. C **70**, 065806 (2004).
[9] C. J. Horowitz, M. A. Pérez-García, D. K. Berry, and J. Piekarewicz, Phys. Rev. C **72**, 035801 (2005).
[10] C. J. Horowitz and D. K. Berry, Phys. Rev. C **78**, 035806 (2008).
[11] C. J. Horowitz, D. K. Berry, C. M. Briggs, M. E. Caplan, A. Cumming, and A. S. Schneider, Phys. Rev. Lett. **114**, 031102 (2015).
[12] A. S. Schneider, D. K. Berry, C. M. Briggs, M. E. Caplan, and C. J. Horowitz, Phys. Rev. C **90**, 055805 (2014).
[13] A. S. Schneider, D. K. Berry, M. E. Caplan, C. J. Horowitz, and Z. Lin, Phys. Rev. C **93**, 065806 (2016).
[14] R. Nandi and S. Schramm, The Astrophysical Journal **852**, 135 (2018).
[15] G. Watanabe, K. Iida, and K. Sato, Nuclear Physics A **687**, 512 (2001).
[16] H. Sonoda, G. Watanabe, K. Sato, T. Takiwaki, K. Yasuoka, and T. Ebisuzaki, Phys. Rev. C **75**, 042801 (2007).
[17] M. D. Alloy and D. P. Menezes, Phys. Rev. C **83**, 035803 (2011).
[18] J. Piekarewicz and G. T. Sánchez, Phys. Rev. C **85**, 015807 (2012).
[19] P. N. Alcain, P. A. Giménez Molinelli, and C. O. Dorso, Phys. Rev. C **90**, 065803 (2014).
[20] U. J. Furtado, S. S. Avancini, J. R. Marinelli, W. Martarello, and C. Providência, The European Physical Journal A **52**, 290 (2016).
[21] P. Alcain and C. Dorso, Nuclear Physics A **961**, 183 (2017).
[22] R. Ogasawara and K. Sato, Progress of Theoretical Physics **68**, 222 (1982).
[23] R. Ogasawara, Progress of Theoretical Physics **73**, 367 (1985).
[24] W. G. Newton and J. R. Stone, Phys. Rev. C **79**, 055801 (2009).
[25] G. Watanabe, H. Sonoda, T. Maruyama, K. Sato, K. Yasuoka, and T. Ebisuzaki, Phys. Rev. Lett. **103**, 121101 (2009).
[26] C. J. Horowitz, D. K. Berry, M. E. Caplan, T. Fischer, Z. Lin, W. G. Newton, E. O'Connor, and L. F. Roberts, (2016), arXiv:1611.10226 [astro-ph.HE].
[27] A. Roggero, J. Margueron, L. F. Roberts, and S. Reddy, Phys. Rev. C **97**, 045804 (2018).
[28] C. Pethick and A. Potekhin, Phys. Lett. B **427**, 7 (1998).
[29] G. Watanabe, K. Iida, and K. Sato, Nuclear Physics A **676**, 455 (2000).
[30] P. Magierski and P.-H. Heenen, Phys. Rev. C **65**, 045804 (2002).
[31] M. Gearheart, W. G. Newton, J. Hooker, and B.-A. Li, Mon. Not. Royal Astron. Soc. **418**, 2343 (2011), arXiv:1106.4875 [astro-ph.SR].
[32] J. A. Pons, D. Viganò, and N. Rea, Nat. Phys. **9**, 431 (2013).
[33] H. Pais and C. Providência, Phys. Rev. C **94**, 015808 (2016).
[34] H. Pais, A. Sulaksono, B. K. Agrawal, and C. Providência, Phys. Rev. C **93**, 045802 (2016).
[35] A. Passamonti and J. A. Pons, Monthly Notices of the Royal Astronomical Society **463**, 1173 (2016).
[36] W. G. Newton, K. Murphy, J. Hooker, and B.-A. Li, The Astrophysical Journal Letters **779**, L4 (2013).
[37] R. L. Merritt, E. M. Cackett, E. F. Brown, D. Page, A. Cumming, N. Degenaar, A. Deibel, J. Homan, J. M. Miller, and R. Wijnands, The Astrophysical Journal **833**, 186 (2016).
[38] E. F. Brown, A. Cumming, F. J. Fattoyev, C. J. Horowitz, D. Page, and S. Reddy, Phys. Rev. Lett. **120**, 182701 (2018).
[39] A. Cumming, E. F. Brown, F. J. Fattoyev, C. J. Horowitz, D. Page, and S. Reddy, Phys. Rev. C **95**, 025806 (2017).
[40] A. Deibel, A. Cumming, E. F. Brown, and S. Reddy, The Astrophysical Journal **839**, 95 (2017).
[41] M. E. Caplan, A. S. Schneider, C. J. Horowitz, and D. K. Berry, Phys. Rev. C **91**, 065802 (2015).
[42] P. N. Alcain and C. O. Dorso, Phys. Rev. C **97**, 015803 (2018).
[43] (LIGO Scientific Collaboration and Virgo Collaboration), The Astrophysical Journal **839**, 12 (2017).
[44] M. E. Caplan, A. S. Schneider, and C. J. Horowitz, Phys. Rev. Lett. **121**, 132701 (2018).
[45] M. E. Caplan and C. J. Horowitz, Rev. Mod. Phys. **89**, 041002 (2017).
[46] T. Maruyama, K. Niita, K. Oyamatsu, T. Maruyama, S. Chiba, and A. Iwamoto, Phys. Rev. C **57**, 655 (1998).
[47] T. Maruyama, T. Tatsumi, D. N. Voskresensky, T. Tanigawa, S. Chiba, and T. Maruyama, "Coulomb screening effect on the nuclear-pasta structure," in *Origin of Matter and Evolution of Galaxies 2003* (WORLD SCIENTIFIC, 2012) pp. 417–426.
[48] T. Maruyama, T. Tatsumi, D. N. Voskresensky, T. Tanigawa, and S. Chiba, Phys. Rev. C **72**, 015802 (2005).
[49] C. O. Dorso, P. A. Giménez Molinelli, and J. A. López, Phys. Rev. C **86**, 055805 (2012).
[50] A. S. Schneider, C. J. Horowitz, J. Hughto, and D. K.

Berry, Phys. Rev. C **88**, 065807 (2013).

[51] C. Dorso, G. Frank, and J. Lpez, Nuclear Physics A **978**, 35 (2018).

[52] P. N. Alcain, P. A. Giménez Molinelli, J. I. Nichols, and C. O. Dorso, Phys. Rev. C **89**, 055801 (2014).

[53] R. Nandi and S. Schramm, Phys. Rev. C **94**, 025806 (2016).

[54] S. S. Avancini, M. Ferreira, H. Pais, C. Providência, and G. Röpke, Phys. Rev. C **95**, 045804 (2017).

[55] I. Sagert, G. I. Fann, F. J. Fattoyev, S. Postnikov, and C. J. Horowitz, Phys. Rev. C **93**, 055801 (2016).

[56] S. S. Avancini, D. P. Menezes, M. D. Alloy, J. R. Marinelli, M. M. W. Moraes, and C. Providência, Phys. Rev. C **78**, 015802 (2008).

[57] S. S. Avancini, S. Chiacchiera, D. P. Menezes, and C. Providência, Phys. Rev. C **82**, 055807 (2010).

[58] H. Pais, A. Santos, L. Brito, and C. Providência, Phys. Rev. C **82**, 025801 (2010).

[59] H. Pais, W. G. Newton, and J. R. Stone, Phys. Rev. C **90**, 065802 (2014).

[60] F. Grill, C. Providência, and S. S. Avancini, Phys. Rev. C **85**, 055808 (2012).

[61] S. S. Bao and H. Shen, Phys. Rev. C **89**, 045807 (2014).

[62] N. Alam, H. Pais, C. Providência, and B. K. Agrawal, Phys. Rev. C **95**, 055808 (2017).

[63] F. J. Fattoyev, C. J. Horowitz, and B. Schuetrumpf, Phys. Rev. C **95**, 055804 (2017).

[64] G. Watanabe, K. Sato, K. Yasuoka, and T. Ebisuzaki, Phys. Rev. C **66**, 012801 (2002).

[65] G. Watanabe, K. Sato, K. Yasuoka, and T. Ebisuzaki, Phys. Rev. C **68**, 035806 (2003).

[66] H. Sonoda, G. Watanabe, K. Sato, K. Yasuoka, and T. Ebisuzaki, Phys. Rev. C **77**, 035806 (2008).

[67] R. Nandi and S. Schramm, Phys. Rev. C **95**, 065801 (2017).

[68] H. Pais and J. R. Stone, Phys. Rev. Lett. **109**, 151101 (2012).

[69] H. Pais, S. Chiacchiera, and C. Providência, Phys. Rev. C **91**, 055801 (2015).

[70] B. Schuetrumpf, M. A. Klatt, K. Iida, J. A. Maruhn, K. Mecke, and P.-G. Reinhard, Phys. Rev. C **87**, 055805 (2013).

[71] B. Schuetrumpf, K. Iida, J. A. Maruhn, and P.-G. Reinhard, Phys. Rev. C **90**, 055802 (2014).

[72] G. Watanabe, K. Sato, K. Yasuoka, and T. Ebisuzaki, Phys. Rev. C **69**, 055805 (2004).

[73] M. Okamoto, T. Maruyama, K. Yabana, and T. Tatsumi, Phys. Lett. B **713**, 284 (2012).

[74] M. Okamoto, T. Maruyama, K. Yabana, and T. Tatsumi, Phys. Rev. C **88**, 025801 (2013).

[75] K. Nakazato, K. Oyamatsu, and S. Yamada, Phys. Rev. Lett. **103**, 132501 (2009).

[76] K. Nakazato, K. Iida, and K. Oyamatsu, Phys. Rev. C **83**, 065811 (2011).

[77] B. Schuetrumpf, M. A. Klatt, K. Iida, G. E. Schröder-Turk, J. A. Maruhn, K. Mecke, and P.-G. Reinhard, Phys. Rev. C **91**, 025801 (2015).

[78] B. Schuetrumpf and W. Nazarewicz, Phys. Rev. C **92**, 045806 (2015).

[79] S. Kubis and W. Wjcik, (2017), arXiv:1705.09570 [astro-ph.HE].

[80] R. A. Kycia, S. Kubis, and W. Wójcik, Phys. Rev. C **96**, 025803 (2017).

[81] P. A. Giménez Molinelli, J. I. Nichols, J. A. López, and C. O. Dorso, Nuclear Physics A **923**, 31 (2014).

[82] P. G. Molinelli and C. Dorso, Nuclear Physics A **933**, 306 (2015).

[83] P. A. Giménez Molinelli and C. O. Dorso, Nuclear Physics A **933**, 306 (2015).

[84] D. N. Kobyakov, (2017), arXiv:1710.02018 [nucl-th].

[85] R. C. R. de Lima, S. S. Avancini, and C. Providência, Phys. Rev. C **88**, 035804 (2013).

[86] D. D. Ofengeim and D. G. Yakovlev, EPL (Europhysics Letters) **112**, 59001 (2015).

[87] P. Milde, D. Köhler, J. Seidel, L. M. Eng, A. Bauer, A. Chacon, J. Kindervater, S. Mühlbauer, C. Pfleiderer, S. Buhrandt, C. Schütte, and A. Rosch, Science **340**, 1076 (2013), http://science.sciencemag.org/content/340/6136/1076.full.pdf.

[88] M. Kawaguchi, Y.-L. Ma, and S. Matsuzaki, Phys. Rev. C **98**, 035803 (2018).

[89] J. Seddon and R. Templer, Handbook of biological physics **1**, 97 (1995).

[90] S.-J. Marrink and A. E. Mark, Biophysical journal **87**, 3894 (2004).

[91] M. A. Horsch, Z. Zhang, and S. C. Glotzer, Phys. Rev. Lett. **95**, 056105 (2005).

[92] C. Fodor, G. Kali, R. Thomann, Y. Thomann, B. Ivan, and R. Mulhaupt, RSC Adv. **7**, 6827 (2017).

[93] A. A. Lazutin, V. V. Vasilevskaya, and A. R. Khokhlov, Soft Matter **13**, 8525 (2017).

[94] J. López-Sauceda and M. D. Rueda-Contreras, Evolutionary Bioinformatics **13**, 1176934317697978 (2017).

[95] M. Terasaki, T. Shemesh, N. Kasthuri, R. Klemm, R. Schalek, K. Hayworth, A. Hand, M. Yankova, G. Huber, J. Lichtman, T. Rapoport, and M. Kozlov, Cell **154**, 285 (2013).

[96] J. Guven, G. Huber, and D. M. Valencia, Phys. Rev. Lett. **113**, 188101 (2014).

[97] D. K. Berry, M. E. Caplan, C. J. Horowitz, G. Huber, and A. S. Schneider, Phys. Rev. C **94**, 055801 (2016).

[98] D. K. Berry, J. Schuchart, and R. Henschel, "Experiences Porting a Molecular Dynamics Code to GPUs on a Cray XK7," http://hgpu.org/?p=11116, accessed: 2014-11-05.

[99] C. J. Horowitz and J. Hughto, (2008), arXiv:0812.2650 [astro-ph].

[100] J. Huang, J. Jia, and B. Zhang, Computer Physics Communications **180**, 2331 (2009).

[101] B. Zhang, J. Huang, N. P. Pitsianis, and X. Sun, Computer Physics Communications **181**, 2206 (2010).

[102] A. D. Baczewski, D. L. Dault, and B. Shanker, IEEE Transactions on Antennas and Propagation **60**, 4281 (2012).

[103] D. G. Yakovlev, Mon. Not. Royal Astron. Soc. **453**, 581 (2015).

[104] W. Helfrich, Z. Naturforschung **28**, 693 (1973).

[105] W. G. Newton, (unpublished).

[106] V. de la Mota, F. Sbille, and P. Eudes, Journal of Physics: Conference Series **420**, 012146 (2013).

[107] F. Sébille, V. de la Mota, and S. Figerou, Phys. Rev. C **84**, 055801 (2011).

[108] J. Hughto, A. S. Schneider, C. J. Horowitz, and D. K. Berry, Phys. Rev. E **84**, 016401 (2011).

[109] C. Horowitz, (2012), arXiv:1212.6405 [nucl-th].